Furnell, KE, Collins, CA, Kelvin, LS, Baldry, IK, James, PA, Manolopoulou, M, Mann, RG, Giles, PA, Bermeo, A, Hilton, M, Wilkinson, R, Romer, AK, Vergara, C, Bhargava, S, Stott, JP, Mayers, J and Viana, P

The Growth of Intracluster Light in XCS-HSC Galaxy Clusters from 0.1 < z < 0.5

Monthly Notices of the ROYAL ASTRONOMICAL SOCIETY

MNRAS **502,** 2419–2437 (2021)
Advance Access publication 2021 January 11
doi:10.1093/mnras/stab065

The growth of intracluster light in XCS-HSC galaxy clusters from $0.1 < z < 0.5$

Kate E. Furnell,[1★] Chris A. Collins,[1★] Lee S. Kelvin,[1,2] Ivan K. Baldry,[1] Phil A. James,[1] Maria Manolopoulou,[3] Robert G. Mann,[3] Paul A. Giles,[4] Alberto Bermeo,[4] Matthew Hilton,[5,6] Reese Wilkinson,[4] A. Kathy Romer,[4] Carlos Vergara,[4] Sunayana Bhargava,[4] John P. Stott,[7] Julian Mayers[4] and Pedro Viana[8,9]

[1]*Astrophysics Research Institute, Liverpool John Moores University, IC2, Liverpool Science Park, 146 Brownlow Hill, Liverpool L3 5RF, UK*
[2]*Department of Astrophysical Sciences, Princeton University, 4 Ivy Ln, Princeton, NJ 08544, USA*
[3]*Institute for Astronomy, University of Edinburgh, Blackford Hill, Edinburgh EH9 3HJ, UK*
[4]*Department of Physics and Astronomy, University of Sussex, Brighton BN1 9QH, UK*
[5]*Astrophysics Research Centre, University of KwaZulu-Natal, Westville Campus, Durban 4041, South Africa*
[6]*School of Mathematics, Statistics & Computer Science, University of KwaZulu-Natal, Westville Campus, Durban 4041, South Africa*
[7]*Department of Physics, Lancaster University, Lancaster LA1 4YB, UK*
[8]*Instituto de Astrofísica e Ciências do Espaço, Universidade do Porto, CAUP, Rua das Estrelas, P-4150-762 Porto, Portugal*
[9]*Departamento de Física e Astronomia, Faculdade de Ciências, Universidade do Porto, Rua do Campo Alegre, 687, P-4169-007 Porto, Portugal*

Accepted 2021 January 4. Received 2021 January 4; in original form 2019 December 4

ABSTRACT

We estimate the intracluster light (ICL) component within a sample of 18 clusters detected in the *XMM* Cluster Survey (XCS) data using the deep (∼26.8 mag) Hyper Suprime-Cam Subaru Strategic Programme data release 1 *i*-band data. We apply a rest-frame $\mu_{\rm B} = 25\,{\rm mag\,arcsec^{-2}}$ isophotal threshold to our clusters, below which we define light as the ICL within an aperture of $R_{\rm X,500}$ (X-ray estimate of R_{500}) centred on the brightest cluster galaxy (BCG). After applying careful masking and corrections for flux losses from background subtraction, we recover ∼20 per cent of the ICL flux, approximately four times our estimate of the typical background at the same isophotal level (∼5 per cent). We find that the ICL makes up about ∼24 per cent of the total cluster stellar mass on average (∼41 per cent including the flux contained in the BCG within 50 kpc); this value is well matched with other observational studies and semi-analytic/numerical simulations, but is significantly smaller than results from recent hydrodynamical simulations (even when measured in an observationally consistent way). We find no evidence for any links between the amount of ICL flux with cluster mass, but find a growth rate of 2–4 for the ICL between $0.1 < z < 0.5$. We conclude that the ICL is the dominant evolutionary component of stellar mass in clusters from $z \sim 1$. Our work highlights the need for a consistent approach when measuring ICL alongside the need for deeper imaging, in order to unambiguously measure the ICL across as broad a redshift range as possible (e.g. 10-yr stacked imaging from the Vera C. Rubin Observatory).

Key words: galaxies – cosmology – galaxy clusters.

1 INTRODUCTION

A complete understanding of the growth of universal large-scale structure (LSS) is one of the primary goals of modern cosmology. Structures that make up the 'cosmic web' include 'nodes' (gravitationally bound groups and clusters of galaxies), 'filaments' (lower density connective 'strings' of galaxies), and 'voids' (vast underdensities of galaxies). These have been observed extensively in nature, initially by Fritz Zwicky, with widespread cataloguing later by individuals such as George O. Abell in the early-to-mid 20th century (e.g. Zwicky 1937; Abell 1958) to a more extensive scale by modern spectroscopic galaxy surveys (e.g. 2dFGRS; Colless et al. 2001). Our comprehension of how matter – baryonic (protons, neutrons, and electrons) and dark – collapses to form these structures (and the rate at which this happens) is partially governed by our understanding of cosmology (e.g. BAHAMAS; McCarthy et al. 2018).

Effective comparisons between observed cluster properties and outputs from hydrodynamical simulations remain critical when attempting to accurately model LSS. In recent years, cosmological hydrodynamical simulations have been reasonably successful in reproducing the structures observed in nature (e.g. Millennium; Springel et al. 2005; see their fig. 1). However, for example, at individual cluster scales, there are numerous key inconsistencies (e.g. the baryonic matter fraction). This has motivated higher resolution 'zoom' simulations with more complex 'subgrid' physics to better understand these differences (e.g. Barnes et al. 2017b), as well as applying semi-analytic models (SAMs) to simulated dark matter haloes (e.g. De Lucia & Blaizot 2007).

These discrepancies are especially striking in the case of brightest cluster galaxies (BCGs) – massive, often non-star-forming galaxies that primarily reside at the X-ray peak of galaxy clusters, a proxy

★ E-mail: k.e.furnell@liverpool.ac.uk (KEF); c.a.collins@ljmu.ac.uk (CAC)

used for the bottom of the gravitational potential well (e.g. Lin & Mohr 2004). For example, there are unresolved tensions with most cosmological simulations regarding 'profile cuspiness' (e.g. Navarro, Frenk & White 1996), with observed BCGs having a 'core' present in their dark matter density profiles (e.g. Newman et al. 2013b) that cannot readily exist in the Lambda cold dark matter (ΛCDM) paradigm for non-self-interacting dark matter (e.g. Harvey et al. 2017). Vitally, there are also tensions present between the observed stellar mass growth rate of BCGs (e.g. Collins et al. 2009; Burke et al. 2012) and that in simulations (e.g. De Lucia & Blaizot 2007; Laporte et al. 2013), with simulations generally predicting significantly more rapid rates of growth ($\sim$2–4$\times$ since $z\sim 1$) than those observed in nature (although significant improvements with better agreement have been made in recent studies, e.g. Ragone-Figueroa et al. 2018).

One of the proposed 'solutions' to this missing BCG stellar mass problem is analysis of the co-evolution of cluster BCGs with the intracluster light (ICL; e.g. Zwicky 1952; Gunn & Gott 1972; Donzelli, Muriel & Madrid 2011, and numerous others) that is a low-surface brightness (LSB; <1 per cent sky level, e.g. Bernardi et al. 2017), diffuse stellar component in clusters. The origin of the ICL is debated extensively in the literature, namely whether it originates primarily from BCG-passive satellite mergers (e.g. Gonzalez, Zabludoff & Zaritsky 2005; Burke & Collins 2013), tidal stripping from infalling, younger satellites (e.g. Montes & Trujillo 2014, 2018; DeMaio et al. 2015, 2018; Morishita et al. 2017), *in situ* star formation due to intracluster medium (ICM) collapse in the case of gas-rich clusters (Puchwein et al. 2010), or a combination of these.

Exactly how much the ICL contributes to the stellar mass of a cluster at a given epoch is much debated throughout the literature. At present epochs ($z\sim 0$), observational results span over a wide range of values (10–50 per cent) with the same being true for simulations; significant tension, however, also exists between them with respect to the rate of observed ICL growth (e.g. Murante et al. 2007; Dolag, Murante & Borgani 2010; Rudick, Mihos & McBride 2011; Contini et al. 2014; Tang et al. 2018). The reasons behind these deviations are unclear, with sample selection, data quality, and method of measurement all being contributing factors to the scatter. As the ICL is a faint component that is not bound to any one cluster galaxy, a concise definition in an observational context is non-trivial. Some authors attempt to model the light profiles of galaxies to disentangle their haloes from the true ICL (e.g. Gonzalez, Zaritsky & Zabludoff 2007; Morishita et al. 2017), whereas others use an isophotal thresholding technique (e.g. Burke et al. 2012; Burke, Hilton & Collins 2015) or use ellipsoidal masks derived from basic structural parameters to mask cluster objects (e.g. Kron 1980; see Zibetti et al. 2005; DeMaio et al. 2018), or use a wavelet-like approach (e.g. Da Rocha & Mendes de Oliveira 2005; Da Rocha, Ziegler & Mendes de Oliveira 2008; Jimenez-Teja & Dupke 2015; Jiménez-Teja et al. 2018; Ellien et al. 2019). All of these methods have various biases and caveats.

In this work, we study the ICL component of a sample of X-ray-selected galaxy clusters from the *XMM* Cluster Survey (XCS), using deep [$i\sim 26.8$ mag, or 28.3 mag arcsec^{-2} (5σ, 2 arcsec $\times$ 2 arcsec)] Hyper Suprime-Cam Strategic Survey Programme data release (DR) 1 imaging (Aihara et al. 2018b). In doing so, we hope to gain a greater understanding of the nature of the accumulation of stellar mass in the cores of clusters since $z\sim 0.5$. This paper is structured as follows: First, we discuss the parent sample of the clusters used for this study; secondly, we outline our selection and detail our methodology used in quantifying the ICL; lastly, we discuss our results. We adopt, where applicable, a standard ΛCDM concordance cosmology throughout, with $H_0 = 70\,\mathrm{km\,s^{-1}Mpc^{-1}}$, $h_{100} = 0.7$, $\Omega_\Lambda = 0.7$, and $\Omega_\mathrm{M} = 0.3$.

Table 1. A summary table of the average limiting depths for the HSC-SSP survey. In this work, we use the 'Deep' layer in the i band (DR1 area $\sim$26 deg^2).

Layer	Filter	Lim. mag. (5σ, 2 arcsec)
Wide	g, r	26.5, 26.1
Wide	i	25.9
Wide	z, y	25.1, 24.4
Deep	g, r	27.5, 27.1
Deep	i	26.8
Deep	z	26.3
Deep	y	25.3
Ultra Deep	g, r	28.1, 27.7
Ultra Deep	i	27.4
Ultra Deep	z, y	26.8, 26.3

2 DATA

2.1 XCS

XCS (Romer et al. 2001) is an all-sky serendipitous search for galaxy clusters using legacy X-ray data from the *XMM–Newton* space telescope (e.g. Jansen et al. 2001). The first XCS DR in 2012 (Mehrtens et al. 2012) contained X-ray and optical confirmations for 503 galaxy clusters, a third of which were entirely new to the literature. The second XCS public DR (Giles et al., in prep.) increases the number of clusters detected in XCS to $\sim$1300 and overlap with this master catalogue in HSC forms the basis of the sample we use in this work.[1] Due to the considerably less biased means of cluster selection in X-rays than optical surveys coupled with high-angular resolution X-ray imaging (4.1 arcsec), the XCS data are ideal for constructing a representative cluster sample.

In the case of the sample used in this work (Giles et al., in prep.), XCS detections were cross-matched for spectroscopy with the Sloan Digital Sky Survey (SDSS) DR13, VIPERS PDR2, and DEEP2 surveys (Albareti et al. 2017, Guzzo et al. 2014, and Newman et al. 2013a, respectively). Spectroscopic redshifts are assigned to each cluster through application of a biweight location estimator (see Beers, Flynn & Gebhardt 1990) using all galaxies falling within 1.5 arcmin from the XCS centroid from the X-ray Automated Pipeline Algorithm (XAPA; Lloyd-Davies et al. 2011); this redshift centroid is then re-calculated after applying a clip of Δv $\pm$ 3000 km s^{-1} about the initial redshift, within a radius of 1.5 Mpc projected distance from the XAPA centroid (see method described in Hilton et al. 2018). Section 4 details the outcome of the matching process for the sample used here.

3 HYPER SUPRIME-CAM SUBARU STRATEGIC PROGRAMME

3.1 Survey description

In this work, we make use of optical imaging data from the first release of the Hyper Suprime-Cam Subaru Strategic Program (HSC-SSP; e.g. Aihara et al. 2018a), one of the deepest, public ground-based optical surveys available (see Table 1). The HSC instrument is a wide-field (1.8 deg^2) imaging camera on the 8.2 m Subaru telescope on Mauna Kea, Hawaii where the SSP has been running

[1] A comparison between the HSC footprint and other surveys can be found here: https://hsc.mtk.nao.ac.jp/ssp/survey/.

since 2014 March. In total, the SSP is scheduled for a run of 300 nights over the course of 6 yr, covering three imaging depths in total: 'Wide', 'Deep', and 'Ultra-Deep' in five Sloan-like passbands (*grizy*). In this work, we use imaging from the 'Deep' subset, chosen to keep the imaging data for our cluster sample as consistently deep as possible. A summary table of the average 5σ limiting depths has been included for reference for the available runs and broadbands (Table 1). The survey footprint overlaps with numerous other surveys, such as the general Sloan footprint and its associated surveys (e.g. York et al. 2000), Pan-STARRS (e.g. Chambers et al. 2016), COSMOS (e.g. Scoville et al. 2007), and DEEP-2 (e.g. Newman et al. 2013a). The imaging depth of HSC far exceeds that of any current public survey (e.g. KiDS, de Jong et al. 2013; DES, Flaugher 2005), with the exception of the Hubble Frontier Fields (Lotz et al. 2017). Current estimates of HSC image quality are comparable to surveys anticipated by the upcoming Vera C. Rubin Observatory (formerly the Large Synoptic Survey Telescope; see Ivezic et al. 2008 and Brough et al. 2020, also Section 3.2 for further comments on data reduction).

3.2 Data reduction

For the DR1 release, the HSC-SSP data products have undergone processing through the HSC pipeline, an adapted version of the Vera C. Rubin Observatory Data Management (DM) software stack in preparation for Vera C. Rubin Observatory data products in the coming decade (see Jurić & Tyson 2012, for a description of the Vera C. Rubin Observatory DM stack). The full implementation for HSC is detailed in Bosch et al. (2018) (including a flow diagram of the complete process; see their fig. 1) but we include an abridged version here to provide context. The pipeline software itself is open source and licensed for public use under the GNU public license (version 3). The photometric performance of the pipeline on mock objects is described in detail in Huang et al. (2018a), who demonstrate a strong recovery in input versus output flux even for de Vaucouleurs-like objects (on average ~85 per cent at $m_i = 25$). They acknowledge, however, that the HSC pipeline tends to oversubtract flux around extended, bright objects (which they explore further when studying the faint haloes of elliptical-type galaxies in Huang et al. 2018b). We discuss this issue, along with a proposition of a post-processing 'fix', in Section 5.1.

In simplified terms, much of the HSC pipeline is built on algorithms and concepts originating from the SDSS *photo* pipeline (see Lupton et al. 2001), the pipeline that produces the data products for all SDSS DRs. Raw data and coadds can be queried online on the HSC-SSP DR1 release site; alternatively, there are reduced data products (e.g. photometry, best-fitting models, and photo-z estimates) available that can be downloaded via SQL query.

The HSC pipeline operates in several stages to produce the final scientific data products. The process (with relevant details) is roughly as follows:

(i) **CCD processing:** the raw data from each CCD are taken, and basic data corrections and calibrations are applied. First, an instrument signature removal is applied, which embodies basic reduction (i.e. flat, bias, and dark corrections), brighter–fatter corrections (for source intensity dependence on the measured PSF), corrections for cross-talk, and corrections for CCD non-linearity (see e.g. Krick & Bernstein 2007, for context as to how this applies to ICL). The sky is estimated for each image and subtracted using a variance-weighted sixth-order Chebyshev polynomial sampled over 128 × 128 3σ clipped average pixel values.

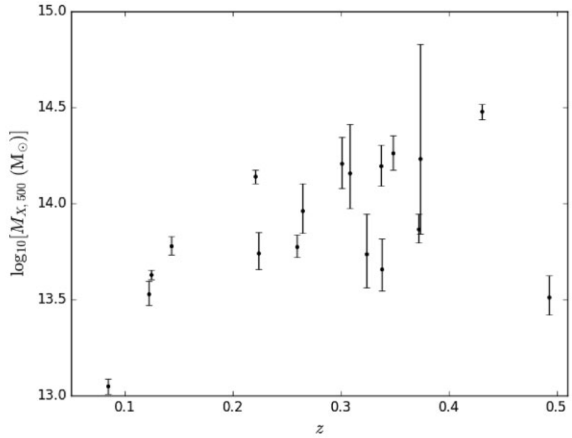

Figure 1. The $M_{X,500}$–z relation for the clusters used in this work (see the text for details). The redshifts are spectroscopic, with errors of $\Delta z \sim 10^{-5}$. The clusters span a wide range in both redshift and mass; a correlation is detected, but it is not significant (see Table 5).

In summary, this stage produces two main data products: calibrated exposure data (i.e. data cubes that contain the following: a background-subtracted, calibrated image; a mask frame containing source detections, pixel flags, and star masks; a variance frame, essentially a 'weight map' describing the pixel-by pixel variance of the coadded images) and a 'source catalogue', namely a data base of detected objects with photometric information as measured by the pipeline.

(ii) **Joint calibration:** When all CCDs have been processed, their astrometric and photometric calibrations are refined by requiring consistent positional and flux values of sources on repeat visits where they may appear on different regions of the focal plane.

(iii) **Image coaddition:** The individual CCD exposures are then coadded to improve the imaging depth. As is widely known in astronomical surveys, coaddition can lead to complications, such as data degradation or introduction of systematic errors. Efforts have been made during the HSC pipeline's construction to avoid these issues wherever possible; as stressed by Bosch et al. (2018), the pipeline is still actively undergoing refinement.

(iv) **Coadd processing:** After creating the coadds, the pipeline carries out another round of image processing. Objects on the coadds are detected, deblended, and measured, creating a catalogue of final object measurements. A final background is then subtracted for each sky 'patch' via an average from a 4k × 4k pixel bin.

4 SAMPLE SELECTION

To create our sample of clusters; the corresponding $M_{X,500}$–z relation (see Section 5.5) can be seen in Fig. 1, we cross-matched the XCS-DR2 North (Giles et al., in prep.) master source list with the entire HSC-SSP DR1 footprint region (Wide, Deep, and Ultra-Deep). This produced an initial match of 202 common sources. We required, for robustness, for there to be an available spectroscopic redshift for both the assigned BCG and for the cluster itself; 79 objects met this criterion. The BCGs in this work are assigned through the GMPhorCC algorithm of Hood & Mann (2017) and then eyeballed individually using optical images with overlaid X-ray contours. The GMPhorCC algorithm models galaxy distributions as Gaussian mixtures using the SDSS DR10 data, using objects from the main galaxy catalogue (see paper for details on colour selection criteria and identifying the red sequence; see also their fig. 4 for a detailed

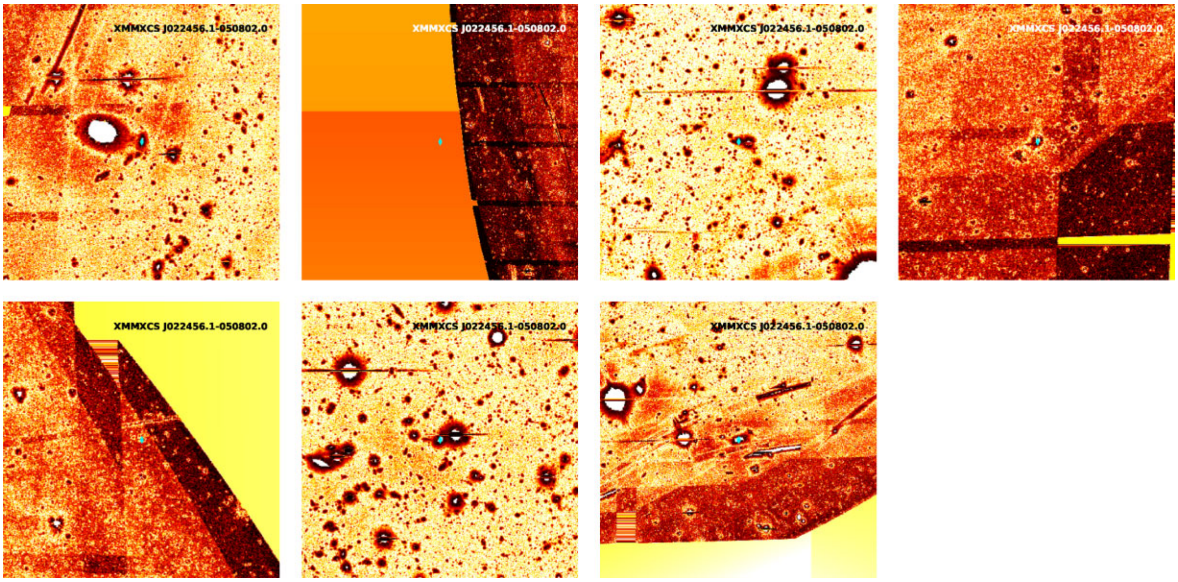

Figure 2. The seven clusters (1.5 × 1.5 Mpc on each frame) omitted from the sample due to poor photometry or bright source contamination. BCGs, if present on the frame, are marked with cyan diamonds. The images have been log-scaled and Gaussian-smoothed to show structure.

flowchart on the operation of the algorithm). From this, it was decided that no reassignments were necessary.

The BCG and cluster spectroscopic redshifts were then compared – if they deviated significantly from one another beyond a specified velocity space limit ($\Delta v > \pm 5000\,\mathrm{km\,s^{-1}}$), these objects were discarded (8 objects, leaving 71). We then required that each cluster had X-ray source parameter measurements (e.g. X-ray temperature, $T_{\mathrm{X},500}$) from XAPA (53 objects). Finally, to ensure that the depths of our images were approximately consistent, we selected only sources that lie within the HSC-SSP Deep footprint (29 objects).

For each of the fields, *i*-band image data were then downloaded as cut-outs (see Section 3) using a field size equivalent to 1.5 × 1.5 Mpc at the spectroscopic redshift of the cluster. These were checked against the value used here as a proxy for cluster radius (see Section 5.5) to ensure that the field size encompassed the size of the cluster as estimated by X-rays. The quality of the individual fields was checked at this stage, with seven being discarded due to bright foreground source contamination or being at the edge of a field. The seven clusters with rejected image data are shown in Fig. 2. Another four clusters were also rejected a posteriori, as they were agreed by the collaboration to be poor candidates. Our final sample therefore consists of 18 clusters (see Fig. 5). The clusters span a wide range in both redshift ($0.06 < z < 0.5$) and halo mass ($10^{12.5} < M_{\mathrm{X},500} < 10^{14.5}$).

From the X-ray measurements, we estimate $R_{\mathrm{X},500}$ and $M_{\mathrm{X},500}$ using the X-ray temperatures of the remaining clusters in our sample (the subscript X,500 referring to the value being derived from X-rays). $R_{\mathrm{X},500}$ act as a proxy for the cluster radius and are used as physically motivated aperture sizes for measuring ICL; $R_{\mathrm{X},500}$ also has the benefit of lower levels of contamination from the background compared with larger cluster radii (e.g. R_{200}). We do, however, recognize that there is a significant caveat with this method, in that we are assuming the BCG to be a proxy for the centre of the cluster. While this is generally a reasonable assumption at low redshift (e.g. Lin & Mohr 2004), at higher redshift, there are an increasing number of clusters out of dynamical relaxation (e.g. Hatch et al. 2011) with multiple BCG candidates; this may be resolved in future studies with deeper photometric coverage (e.g. mass-weighted centroid estimation via weak lensing).

Both $R_{\mathrm{X},500}$ and $M_{\mathrm{X},500}$ are computed via the scaling relations of Arnaud, Pointecouteau & Pratt (2005), modelled as power laws:

$$E(z)R_{\mathrm{X},500} = 1.104\left[\frac{kT}{5\ \mathrm{keV}}\right]^{0.57}\ \mathrm{Mpc}\,, \tag{1}$$

$$E(z)M_{\mathrm{X},500} = 3.84\times10^{14}\left[\frac{kT}{5\ \mathrm{keV}}\right]^{1.71}\ \mathrm{M}_{\odot}\,, \tag{2}$$

where $T_{\mathrm{X},500}$ is the X-ray temperature (K) and $E(z)$ here is

$$E(z) = [\Omega_{\mathrm{M}}(1+z)^3 + \Omega_{\Lambda}]^{-1/2}, \tag{3}$$

where z is the cluster redshift and Ω_{M} and Ω_{Λ} are our concordance cosmology values. The range of $R_{\mathrm{X},500}$ and $M_{\mathrm{X},500}$ values for our clusters is summarized in Table 2. Although we recognize that the relation from Arnaud et al. (2005) is derived from relaxed clusters (which may not be the case here), a recent paper from Giles et al. (2017) investigated the luminosity–mass relation using the statistically complete *Chandra* data with masses derived via a hydrostatic mass analysis. They found no significant differences between relaxed and non-relaxed clusters when comparing masses derived from a Y_x–mass relation.

5 ANALYSIS

5.1 Background oversubtraction – the 'divot correction' method

A major concern regarding the measurement of ICL is not only the *addition* of flux from excess sources (as discussed in the prior section and in Section 5.4) but also the *oversubtraction* of flux. For space-based telescopes with low levels of background, this is generally less of a concern [e.g. *Hubble Space Telescope* (*HST*)]; in the case of ground-based telescopes, however, it provides a significant challenge for LSB science. For extended objects such as galaxies, issues arise due to modern commonly used background estimation methods, namely spline-mesh approaches. Within the

Table 2. The main parameters of the 18 XCS-HSC clusters used in this work. The BCG rest-frame *i*-band absolute magnitudes (M_i) are derived from aperture values as described in Section 5.2. The relative errors are derived using the HSC variance maps and are typically quite small ($\Delta M_{\mathrm{i}} < 0.01$ mag).

XCS ID	α_{2000}	δ_{2000}	z	M_i	$T_{\mathrm{X},500}$ (keV)	$R_{\mathrm{X},500}$ (Mpc)	$M_{\mathrm{X},500}$ ($10^{14}\times \mathrm{M}_{\odot}$)
XMMXCS J022456.1−050802.0	36.234	− 5.134	0.0840	−23.023	0.648 ± 0.034	0.331 ± 0.010	0.112 ± 0.010
XMMXCS J161039.2+540604.0	242.664	+54.101	0.339	−23.718	$1.595 \pm^{+0.373}_{-0.227}$	$0.483 \pm^{0.041}_{0.062}$	$0.457 \pm^{0.198}_{0.105}$
XMMXCS J233137.8+000735.0	352.908	+0.126	0.224	−23.690	$1.719 \pm^{+0.269}_{-0.184}$	$0.537 \pm^{0.033}_{0.046}$	$0.553 \pm^{0.156}_{0.971}$
XMMXCS J232923.6−004854.7	352.348	− 0.815	0.300	−23.882	$3.292 \pm^{+0.677}_{-0.524}$	$0.746 \pm^{0.070}_{0.084}$	$1.611 \pm^{0.608}_{0.413}$
XMMXCS J161134.1+541640.5	242.892	+54.278	0.337	−24.009	$3.278 \pm^{+0.511}_{-0.429}$	$0.729 \pm^{0.056}_{0.063}$	$1.567 \pm^{0.441}_{0.334}$
XMMXCS J095902.7+025544.9	149.761	+2.929	0.349	−23.534	$3.609 \pm^{+0.472}_{-0.400}$	$0.765 \pm^{0.050}_{0.056}$	$1.836 \pm^{0.429}_{0.335}$
XMMXCS J095901.2+024740.4	149.755	+2.794	0.501	−23.587	$1.385 \pm^{+0.223}_{-0.167}$	$0.406 \pm^{0.029}_{0.036}$	$0.327 \pm^{0.095}_{0.064}$
XMMXCS J100141.6+022538.8	150.424	+2.427	0.124	−23.752	$1.427 \pm^{+0.049}_{-0.045}$	0.509 ± 0.010	$0.424 \pm^{0.025}_{0.022}$
XMMXCS J095737.1+023428.9	149.405	+2.575	0.373	−24.652	$3.500 \pm^{+4.291}_{-1.443}$	$0.741 \pm^{0.194}_{0.423}$	$1.716 \pm^{5.027}_{1.025}$
XMMXCS J022156.8−054521.9	35.487	− 5.756	0.259	−23.619	$1.814 \pm^{+0.157}_{-0.129}$	$0.544 \pm^{0.022}_{0.026}$	$0.595 \pm^{0.091}_{0.071}$
XMMXCS J022148.1−034608.0	35.450	− 3.769	0.432	−23.963	$4.949 \pm^{+0.278}_{-0.245}$	$0.873 \pm^{0.025}_{0.028}$	$3.001 \pm^{0.294}_{0.250}$
XMMXCS J022530.8−041421.1	36.378	− 4.239	0.143	−23.294	$1.761 \pm^{+0.122}_{-0.103}$	$0.568 \pm^{0.019}_{0.022}$	$0.602 \pm^{0.073}_{0.059}$
XMMXCS J100047.3+013927.8	150.197	+1.658	0.221	−23.710	$2.933 \pm^{+0.143}_{-0.137}$	$0.730 \pm^{0.019}_{0.020}$	$1.382 \pm^{0.117}_{0.108}$
XMMXCS J022726.5−043207.1	36.861	− 4.535	0.308	−23.662	$3.090 \pm^{+1.273}_{-0.677}$	$0.716 \pm^{0.100}_{0.160}$	$1.438 \pm^{1.156}_{0.496}$
XMMXCS J022524.8−044043.4	36.353	− 4.679	0.264	−23.244	$2.339 \pm^{+0.492}_{-0.343}$	$0.626 \pm^{0.054}_{0.072}$	$0.917 \pm^{0.354}_{0.218}$
XMMXCS J095951.2+014045.8	149.963	+1.679	0.372	−24.057	$2.128 \pm^{+0.238}_{-0.192}$	$0.557 \pm^{0.029}_{0.035}$	$0.734 \pm^{0.146}_{0.110}$
XMMXCS J022401.9−050528.4	36.008	− 5.091	0.324	−23.206	$1.759 \pm^{+0.576}_{-0.364}$	$0.515 \pm^{0.064}_{0.090}$	$0.544 \pm^{0.339}_{0.178}$
XMMXCS J095924.7+014614.1	149.853	+1.770	0.124	−22.717	$1.252 \pm^{+0.113}_{-0.098}$	$0.472 \pm^{0.022}_{0.024}$	$0.339 \pm^{0.054}_{0.044}$

galaxy-modelling literature, this issue is long known (e.g. Zhao, Aragón-Salamanca & Conselice 2015a, and references therein); namely that such approaches produce a 'dearth' of flux around extended sources, termed here as a 'divot'.

Divots occur because we are limited in our background estimation by the size of our chosen mesh, as we cannot accommodate for the wide range of angular extents of all objects in a frame. Hence, some light in extended object profile wings is often mistaken for background flux and mistakenly subtracted with the sky. Even in surveys such as HSC where background estimation is (more or less) state-of-the-art, these features still occur (see Fig. 3). This effect is doubly serious in the case of cluster and ICL science compared with isolated galaxies, as there is often a high source density (i.e. overlapping profile wings), which makes it nearly impossible to select a globally appropriate mesh size.

In an upcoming paper (Kelvin et al., in prep.; Lee Kelvin, priv. comm.), we attempt to address these problems, providing survey comparisons and suggesting potential solutions. To do so, we have produced a pipeline to correct for such flux oversubtraction effects. We acknowledge that post-processing is less preferable than an optimized survey strategy, especially given that our method involves parametric estimates that we attempt to avoid as much as possible when measuring our ICL values (Section 5.5). In this case (and in many others), however, this is not an option for either past or present surveys that have not prioritized LSB science in their observational approach. The construction, application, and limits of the aforementioned pipeline will be the subject of a separate paper; here, we instead provide an abridged description of its operation and use in the context of this work.

The pipeline, which is written in R and is primarily SExtractor (version 2.19.5) and SWARP based, operates on an image in three major steps as follows:

(i) **Object detection/modelling:** First, SExtractor is run on a given input image. The settings used are similar to those used in Furnell et al. (2018). Since SExtractor version 2.8 (e.g. Bertin 2009), it is possible to fit models to the light profiles of objects detected by the algorithm. There are several model types available (e.g. delta function, Ferrer profile, exponential profile, and Sérsic profile). Here, we opt for a single-Sérsic model (see equation 4). All detected objects in the frame are modelled with a Sérsic profile, which are fitted through a Levenberg–Marquardt χ^2 minimization algorithm. The Sérsic profile has the following form:

$$I(R) = I_{\mathrm{e}} \exp\{b_n[(R/R_{\mathrm{e}})^{1/n} - 1]\}, \quad (4)$$

where $I(R)$ is the intensity of an object at radius R, R_{e} is the effective radius, I_{e} is the object intensity at the effective radius, n is the Sérsic index, and b_n is a product of incomplete gamma functions as described in Ciotti (1991). SExtractor imposes an internal hard limit on the range of Sérsic indices ($0.5 < n < 8$); the majority in this work fall around $0.5 < n < 4$. The result of doing so is an image frame containing the modelled light profiles of all catalogue objects.

(ii) **Differential inversion:** In order to estimate the flux loss in object profile wings caused during the image processing stage, we then take the difference between the input image and the image containing the object models. The result is then inverted, creating the 'divot correction' (see the centre panel of Fig. 3).

(iii) **Coaddition:** The divot correction image is then added on to the original image using SWARP (LANCZOS3 interpolation; this was selected as recommended in the SWARP user manual, but as the resolution of the images is identical, no resampling is necessary), thus providing an approximate flux 'correction' (see Fig. 3).

There is an obvious caveat in our approach, namely with our selection of a single-Sérsic profile with which we fit to all galaxies in a frame. We therefore assume that object wings will follow those of a Sérsic profile. This estimate is often cuspier than, for example, the true profiles of BCGs, of which some are thought to be multicomponent objects (see e.g. Bernardi et al. 2014; Zhao et al. 2015a; Iodice et al. 2016; Zhang et al. 2019; see also Section 6) and may, for example, lead to residuals that are added into the image,

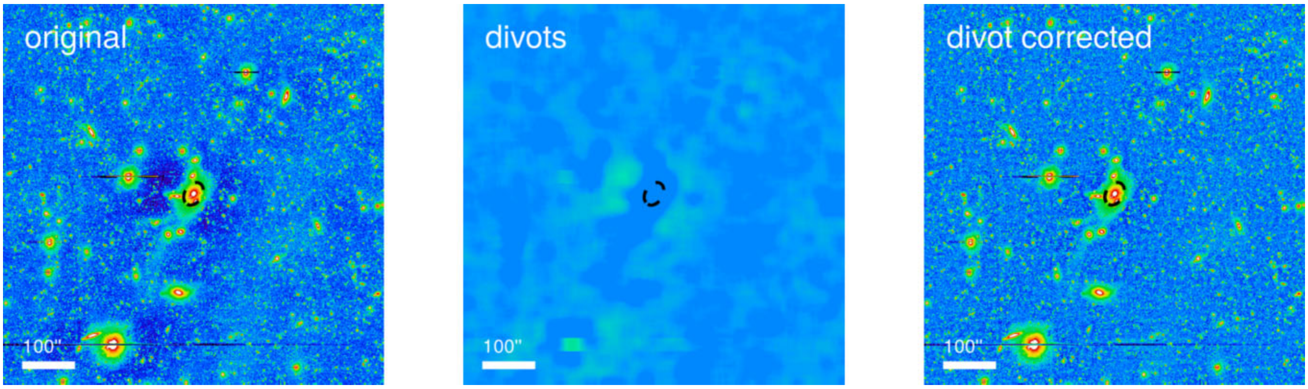

Figure 3. An example of the 'divot correction' method used in this work (shown here for cluster XMMXCS J232923.6–004854.7, $z = 0.3$); all images have the exact same scaling (from Kelvin et al., in prep.). The first image depicts the data prior to correction; as is visible, there is a dearth of flux in the regions around the BCG and its satellites. The second shows the estimated divot correction (the divot corrections are smoothed using a 5-pixel FWHM Gaussian kernel); the third shows the resultant image after implementation. As is visible, there is a vast improvement, with the sky level varying far more smoothly.

which are not part of the divot. As well as this, there will be some dependence on the reliability of the correction with both cluster extent and redshift; with that said, we choose large postage stamps (in excess of $R_{X,500}$ in most cases) when modelling the divots (to provide a sense of scale, the objects modelled here range from ∼2 to 13 arcsec). Although we appreciate the simplicity of this approach, the addition of other components to hundreds of models (as well as attempting to accurately morphologically classify all detected objects in a frame) provides not only significant computational cost challenges, but also adds additional free parameters that may not be necessary for all objects and may lead to less reliable fits (see arguments in Furnell et al. 2018). We therefore instead caution the reader that our estimates represent, most likely, a lower limit estimate on the true value of the total wing flux loss during processing. The divot method allows us to quantify the oversubtraction but is not a substitute for a full pipeline sky-subtraction reduction analysis.

5.2 BCG photometry

We apply three methods of quantifying the flux contribution from our cluster BCGs: total flux within an aperture of radius 50 kpc (e.g. Whiley et al. 2008) or two parametric models: a single, free Sérsic fit or a de Vaucouleurs model with a fixed Sérsic index of 4. We choose an aperture of radius 50 kpc primarily as other authors have found that this radius corresponds approximately to the region where there is an excess of light in BCGs compared with a de Vaucouleurs profile (e.g. Presotto et al. 2014). We prefer, given the nature of our data, to take a simplistic approach over attempting to fit multiple components here. We take a similar approach as in our previous work in this respect (Furnell et al. 2018), where we assessed the performance of the pipeline for the SDSS data. There are numerous arguments as to the best model to fit; most notably, a two-component model that includes the addition of an exponential halo to a Sérsic profile (e.g. Donzelli et al. 2011; Bernardi et al. 2013; Zhao et al. 2015a). However, we take the approach in this work that disentangling the BCG from the ICL is non-trivial to achieve, given how much they are closely linked in terms of evolutionary history (e.g. Burke et al. 2012; Iodice et al. 2016; Spavone et al. 2018), so include parametric model fits primarily as a comparative measure. For our results, due to them being non-parametric, we use the aperture values to represent our BCG fluxes.

We model our galaxies using the SIGMA pipeline (Structural Investigation of Galaxies via Model Analysis; see Kelvin et al. 2012), using a similar implementation as in Furnell et al. (2018). SIGMA is a software wrapper written in R that performs a full model fit of a given object using GALFIT 3 (see Peng et al. 2010), including an estimate of the field PSF using PSFEX (see Bertin 2013). The weight maps used in this procedure are those generated by the HSC pipeline. We fit the BCGs simultaneously with their brightest three neighbours, masking out their centres (to mitigate saturation issues) and the remaining objects in the field. We produce models for our objects pre- and post-divot correction (see Section 5.1) and use the post-divot-corrected models because of the correction to the profile wings of our objects. Generally, the output parameters are similar in both cases (see Fig. 4), and do not show any obvious biases.

It is important to mention that we do not use the PSFs generated by SIGMA when masking of stars on our images (e.g. to estimate the contamination extent); rather, their use is to provide a sufficiently well-approximated model for our BCG model fits. This is because the PSFs generated by SIGMA are not estimated out to large enough radii to account for the wings of the brightest stars on our frames (∼0.2 arcmin). PSFEX is not optimized for the purposes of producing extended PSFs; indeed, using PSFs with a small angular extent both for the purpose of masking and removal of wings from point source contamination represent two of the most commonly cited issues regarding the robustness of LSB photometric studies (e.g. Duc et al. 2015, in the context of deep ATLAS-3D survey data; see also Uson, Boughn & Kuhn 1991; Slater, Harding & Mihos 2009; Trujillo & Fliri 2016; Infante-Sainz, Trujillo & Román 2020; Román, Trujillo & Montes 2020). For a more detailed description of the masking process, see Section 5.3.

In most cases, the three methods of quantifying BCG magnitude agree within a few per cent, with the aperture values generally yielding slightly lower values due to there being no wing extrapolation (e.g. Furnell et al. 2018). There are, however, a couple of cases where there is a disagreement between values of ∼10 per cent or higher:

(i) **XMMXCS J095901.2+024740.4**: the highest redshift system in this work ($z = 0.51$; panel 7 of Fig. 5), with the faintest BCG apparent magnitude from an integrated model ($m_i = 18.51$). The BCG flux fraction for this system with respect to the cluster within $R_{X,500}$ doubles using the best Sérsic fit over either the aperture or de Vaucouleurs values (0.34, compared with 0.17 and 0.21, respectively). From our work in Furnell et al. (2018), we found that

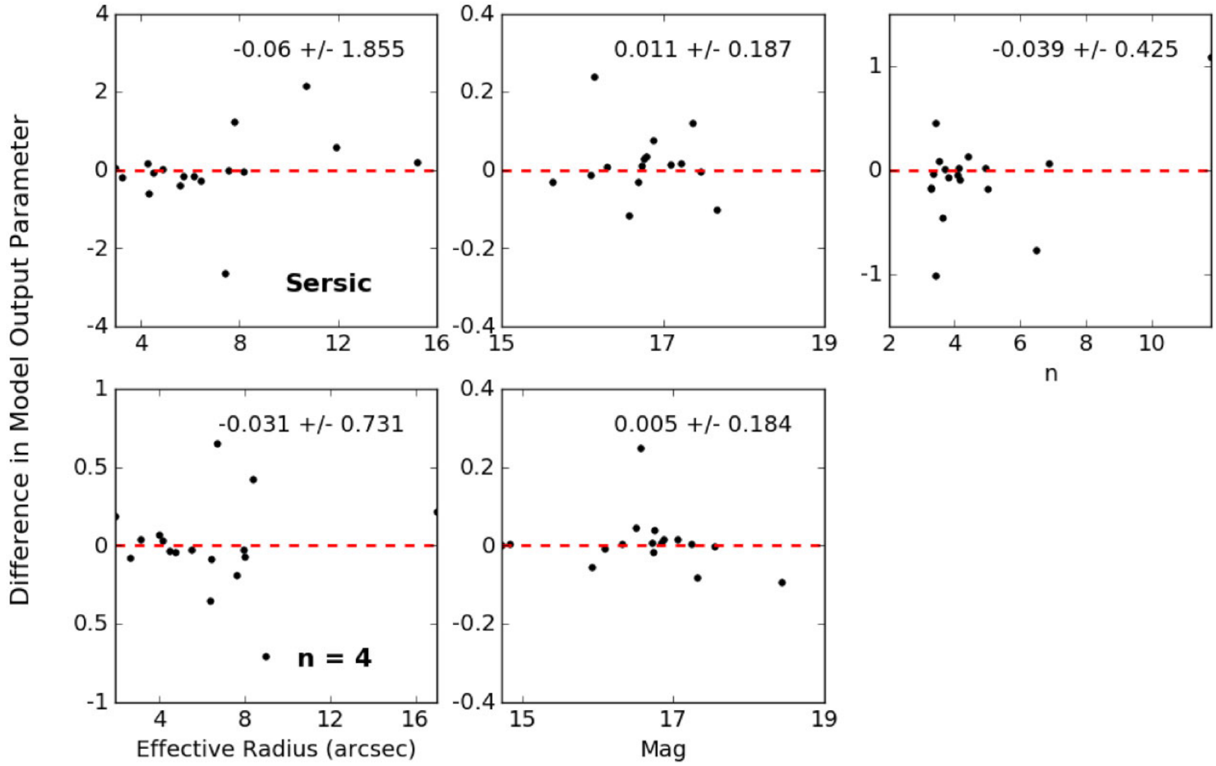

Figure 4. Differential comparison between the input and output parameters for the cluster BCGs in this sample, with and without an added divot correction. The values at the top of each frame represent the median deviation and rms. The top and bottom panels represent the outputs for a free Sérsic profile and a de Vaucouleurs profile, respectively. The fit parameters for both the non-corrected and corrected cases tend to be reasonably similar and there are no clear biases present upon using a divot correction.

galaxy models tended to degrade with decreasing surface brightness; indeed, of all of the BCGs modelled here, the Sérsic fit for this system has the largest relative error.

(ii) **XMMXCS J095951.2+014045.8:** Closer inspection of the system using the DS9 software revealed it to be a cD type (panel 14 of Fig. 5); this extra flux may potentially have been missed through using an aperture to measure the BCG (e.g. for a recent paper on the effect of cD haloes when fitting galaxies, see Zhao, Aragón-Salamanca & Conselice 2015b) and more heavily contributed to the ICL fraction, as both fitted models give a larger fraction of cluster light attributable to the BCG (0.28 in either case, compared with 0.19 for the aperture estimate). As aforementioned, such cases are testament to the caveats of a non-parametric approach.

5.3 Masking

As in every photometric survey, HSC imaging is not free from artefacts. Although the processing algorithm has been optimally designed to avoid such defects wherever possible, some sources of excess flux remain. These include artefacts from overexposed stars, telescope ghosts, satellite trails, and cirrus, to name a few (refer to Duc et al. 2015, for a comprehensive summary). This is shown in Fig. 2, which constitutes examples of clusters in XCS that were not included in the final sample due to heavily contaminated photometry in HSC.

For our sample, we create custom masks in order to minimize the contribution to ICL flux from artefacts. Although the HSC pipeline does produce masks as output, we opt to generate our own as an attempt to more comprehensively remove artefacts, such as extended diffraction spikes from bright stars that are often not cleanly removed. We refer the reader to Bosch et al. (2018) for more details of the masking method used in the HSC pipeline.

For our custom masks, we begin with the binary masks generated by the HSC pipeline. The binary masks contain numerical identifiers in order to differentiate between different 'layers' of the masks, namely artefacts/saturated stars versus objects. From these, we generate our mask layers via the following three stages:

(i) **Bad pixel masking:** We begin by first identifying the 'bad pixel' regions thresholded out by the HSC pipeline. These regions are then masked out, and constitute the first mask layer. These include regions that have been incorrectly weighted by the weight maps, saturated pixels, and some of the artefacts generated by bright stars.

(ii) **Star masking:** Next, we run SEXTRACTOR across all of the images. We set a detection threshold for our objects at 10σ, with other parameters (such as saturation level, etc.) set to roughly the same values as those used during our running of SIGMA. We allow SEXTRACTOR to approximate a rough background level using a large mesh size to account for any extended bright sources (128 pixels). The purpose of this step is primarily to identify brighter, more compact objects within the frame, for which we do not require absolutely accurate photometry.

For fainter stars, we query the *Gaia* DR2 catalogue (Gaia Collaboration 2018) for both photometry and astrometry. The *Gaia* mission aims to collect both photometry and astrometry for $\sim 10^9$ stars in the Milky Way (for science objectives, see Gaia Collaboration 2016). We produce catalogues of stars within the frames of our images, and mask stars out with $17 < G < 21$ (mean apparent magnitude value in the G band from *Gaia*, see technical paper for the filter

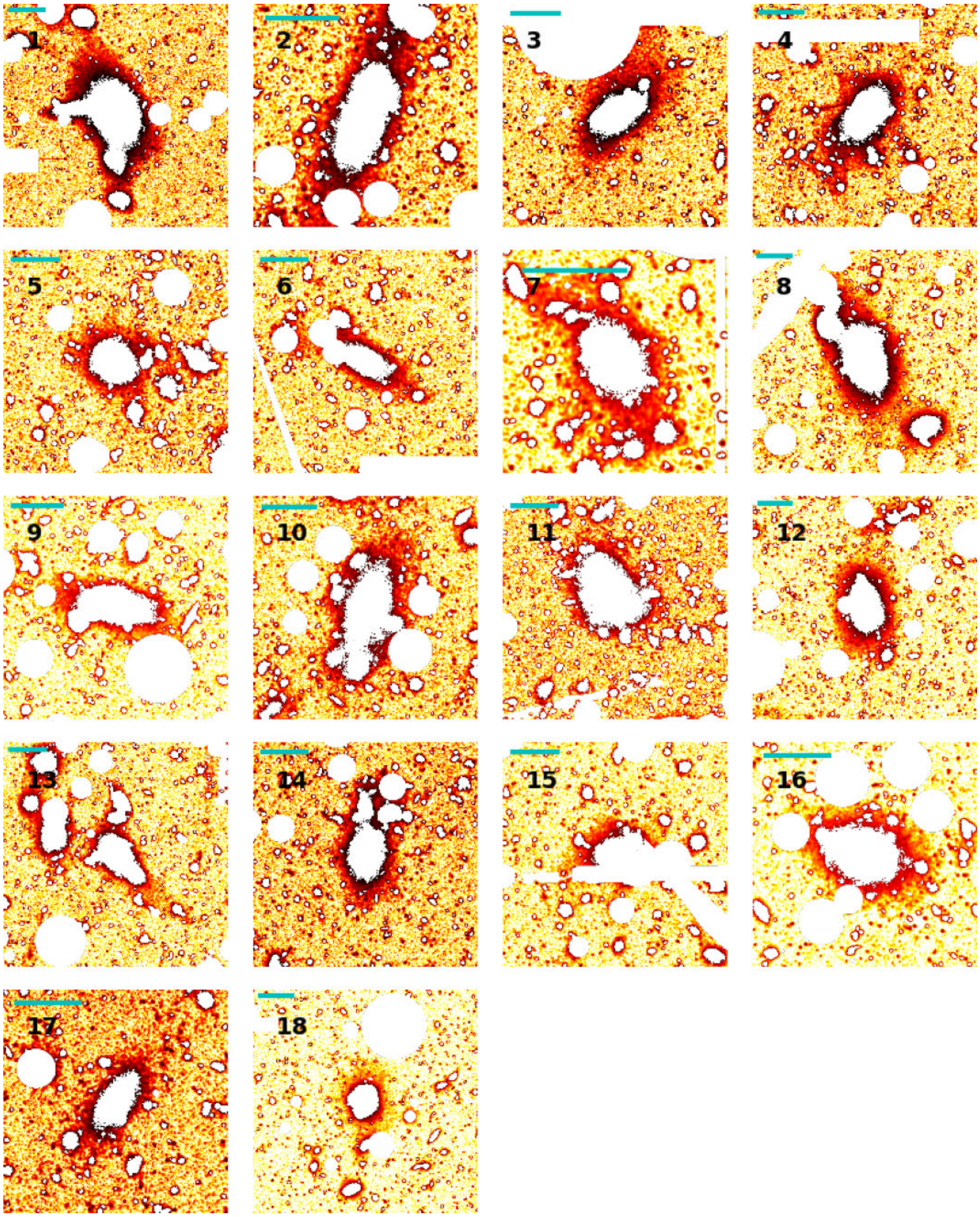

Figure 5. The final equivalent 25 mag arcsec^{-2} masked and divot-corrected images (numerical labels have been included for clarity in discussion), zoomed to 40 per cent of the $R_{X,500}$ value of each respective cluster centred on the BCG (with the exception of panel 7). The cyan line at the top left of each panel is the equivalent 30 arcsec pixel scale for each image. To show structure, the images have been log-scaled and smoothed.

curve: Jordi et al. 2010; $G \sim 21$ is the survey limit). There is around a 10 per cent rate of contamination in *Gaia* by elliptical galaxies; we follow the prescription outlined in Koposov, Belokurov & Torrealba (2017) and apply a cut using the 'astrometric excess noise' parameter, *ans* [$\log_{10}(ans) < 0.15(G - 15) + 0.25$], which they found to be ∼95 per cent effective; upon visual inspection, none of the BCGs were masked in this way. We then apply the following empirical masking formula used canonically in HSC[2] to define our exclusion apertures:

$$r = A_0 \times 10^{B_0(C_0-i)} + A_1 \times 10^{B_1(C_1-i)}, \quad (5)$$

where r is in pixels, i are the HSC i-band magnitudes as measured by SExtractor (Kron aperture, Kron 1980), and $A_0 = 200$, $B_0 = 0.25$, $C_0 = 7.0$, $A_1 = 12.0$, $B_1 = 0.05$, and $C_1 = 16.0$.

For brighter stars ($G < 17$ in our case), this approach is not recommended. Although some bright stars are masked in HSC already, there are many missing due to the prior use of the much less complete NOMAD survey (Zacharias et al. 2004) compared with the *Gaia* survey, which will be used for future releases as detailed in Coupon et al. (2018). Instead, we create custom masks across all frames by hand for the brightest stars, any other point-like sources missed in our catalogues from *Gaia* and any visible diffraction spikes (a similar method to that used, for example, in Montes & Trujillo 2018 and Burke et al. 2015). Using the same method, we also mask

[2] https://hsc-release.mtk.nao.ac.jp/doc/index.php/bright-star-masks/

Table 3. The k-correction ($k_{i,B}$), cosmological dimming and equivalent B-band surface brightness limits at which we observe (where $\mu_{i,\mathrm{obs}}$ is equivalent to $\mu_{B,\mathrm{rest}} = 25$) our clusters, used to generate isophotal masks.

XCS ID	$k_{i,B}(z)$	$2.5\log_{10}(1+z)^4$	$\mu_{i,\mathrm{obs}}$
XMMXCS J022456.1−050802.0	−1.566	0.350	23.784
XMMXCS J161039.2+540604.0	−1.304	1.263	24.959
XMMXCS J233137.8+000735.0	−1.428	0.877	24.450
XMMXCS J232923.6−004854.7	−1.350	1.142	24.792
XMMXCS J161134.1+541640.5	−1.304	1.263	24.958
XMMXCS J095902.7+025544.9	−1.289	1.299	25.010
XMMXCS J095901.2+024740.4	−1.105	1.741	25.635
XMMXCS J100141.6+022538.8	−1.523	0.508	23.985
XMMXCS J095737.1+023428.9	−1.257	1.378	25.121
XMMXCS J022156.8−054521.9	−1.392	1.001	24.608
XMMXCS J022148.1−034608.0	−1.183	1.556	25.374
XMMXCS J022530.8−041421.1	−1.498	0.580	24.082
XMMXCS J100047.3+013927.8	−1.430	0.865	24.435
XMMXCS J022726.5−043207.1	−1.341	1.168	24.827
XMMXCS J022524.8−044043.4	−1.387	1.018	24.631
XMMXCS J095951.2+014045.8	−1.259	1.374	25.115
XMMXCS J022401.9−050528.4	−1.324	1.218	24.894
XMMXCS J095924.7+014614.1	−1.525	0.500	23.975

out all non-cluster galaxies brighter than the BCG via careful visual inspection of the cluster field, following Burke et al. (2015). We used the SAO DS9 imaging software to view our images, which includes an array of tools for image visualization ideal for these purposes, including optimized Gaussian smoothing kernels and high contrast scaling (useful for scaling masks to accommodate stellar wings). Masks were then created by hand using the region definition tool in DS9, and subsequently converted to fit format using the open-source MKMASK software (courtesy: Rolf Janssen).

(iii) **Isophotal mask creation**: We then produce isophotal masks for each of our frames (see discussion in 5.5), below which we define the ICL to be measured and apply these in conjunction with our bad pixel and star masks when performing photometry. To do so, we use an effective surface brightness detection threshold in the rest frame of 25 mag arcsec^{-2} (an approach similar to that carried out on the CLASH cluster sample by Burke et al. 2015). To compare our results with Burke et al. (2015), we also shift our equivalent surface brightness threshold at which we measure ICL to that of the rest-frame B band. For the B-band equivalent threshold, we introduce the following equation:

$$\mu_{i,\mathrm{obs}} = \mu_{B,\mathrm{rest}} + 2.5\log_{10}(1+z)^4 + k_{i,B}(z)\,, \tag{6}$$

where $\mu_{i,\mathrm{obs}}$ is the limit at which we observe, $\mu_{B,\mathrm{rest}}$ is the equivalent rest-frame surface brightness in the B band, $2.5\log_{10}(1+z)^4$ is the bolometric cosmological surface brightness dimming term, and $k_{i,B}(z)$ is the k-correction term, defined here as

$$k_{i,B}(z) = M_{i,\mathrm{obs}}(z) - M_{B,\mathrm{rest}}(z)\,, \tag{7}$$

where $M_{i,\mathrm{obs}}(z)$ and $M_{B,\mathrm{rest}}(z)$ are the pseudo-absolute magnitudes derived for each respective waveband at a given redshift for our choice of stellar population synthesis model. These are computed via the EZGAL software (Mancone & Gonzalez 2012), assuming an old stellar population with a formation redshift of $z_\mathrm{f} = 3$, solar metallicity ($Z_\odot$), and passive evolution thereafter, using the models of Bruzual & Charlot (2003) coupled with a Chabrier (2003) initial mass function (IMF; also resembling the methodology of DeMaio et al. 2018). We list our B-band limits in Table 3.

While we appreciate that it is unlikely that the stars contained within our BCGs evolved entirely *in situ*, most BCGs have shown little evidence for significant growth through starburst activity at $z < 1$ and are primarily assumed to gain mass through mergers with satellites containing reasonably similar stellar populations (or even more passive, e.g. Guo et al. 2009), so we consider this assumed 'burst' model reasonable for simplicity (this was an assumption also made by Burke et al 2015). There are, however, an increasing number of studies showing a younger age for the ICL component compared to the BCG (see, for example, Montes & Trujillo 2014; Morishita et al. 2017; Montes & Trujillo 2018; Jiménez-Teja et al. 2019). As an aside, we also performed an additional check to ensure that correcting to the B band did not result in any serious biases from the rapid fade of bluer stellar populations with redshift (see the appendix).

We show how the choice of metallicity and formation redshift affects our $k_{i,B}(z)$ values in the appendix (Tables A1 and A2), for the mean values of our sample split in two bins about the mean redshift ($0 < z < 0.28$ and $0.28 < z < 0.5$, respectively); in short, there is an *rms* of ±0.3 mag in $k_{i,B}(z)$, depending on the model of choice. Through interpolation (see Section 6.1), this translates at 25 mag arcsec^{-2} to a difference in ±5 per cent of the final ICL value.

5.4 Quantifying the systematic background

In all astronomical image data, a systematic background exists. At visible wavelengths, it is partially caused by faint galaxies below the survey limit (which is a caveat to our method; refer to discussion below), the wings of bright sources such as stars or contaminant galaxies and residual flux from the sky (e.g. Guglielmetti, Fischer & Dose 2009). In order to better understand this in the context of our image data, we performed a test by applying photometry on injected mock profiles so that we could trace the additional flux contribution at a given surface brightness. We performed this test on 'control' frames offset from each of the clusters in this study. The 18 control frames selected were patches of sky within the HSC-SSP footprint, offset at random by 0.5° from the centre of the original frames. We chose to use representative control frames so as to prevent any contributions from ICL that may be present. The control frames were subject to an identical masking method as that used in the cluster frames, were weighted using the HSC-generated weight maps (inverse variance), and were not divot corrected.

For each of the frames, 10 random positions were selected. To mimic an ICL-like profile (found by numerous authors to be approximately exponential, e.g. Seigar, Graham & Jerjen 2007; Zhang et al. 2019), we generated an exponential model ($n = 1$, $R_\mathrm{e} = \langle R_{\mathrm{X},500}\rangle/4$, $\theta = 50°$, $a/b = 0.8$ for Sérsic index, effective radius, position angle, and axial ratio, respectively) at nine surface brightness levels (24–28 mag arcsec^{-2} in steps of 0.5 mag arcsec^{-2}, where, for reference, the faintest limit is ∼3 mag below that which we measure for the ICL in our clusters). The profiles were convolved with the field PSF from SIGMA (as per the modelling process for the BCGs) and an idealized Poisson noise component was added. We injected the models at 10 random positions within each of the control frames, measuring the difference between the input and output flux values using a fixed circular aperture equivalent to the selected effective radius of our models (∼2000 models in total; for a similar method, see Burke et al. 2012).

Fig. 6 shows the bulk output across the fields, with Fig. 7 showing the stacked median for all of the control frames. From our mock photometry, we detect a <5 per cent excess of the input flux on average for an ICL-like profile over the range of our B-band equivalent surface brightness levels (23.74–25.64 mag arcsec^{-2}).

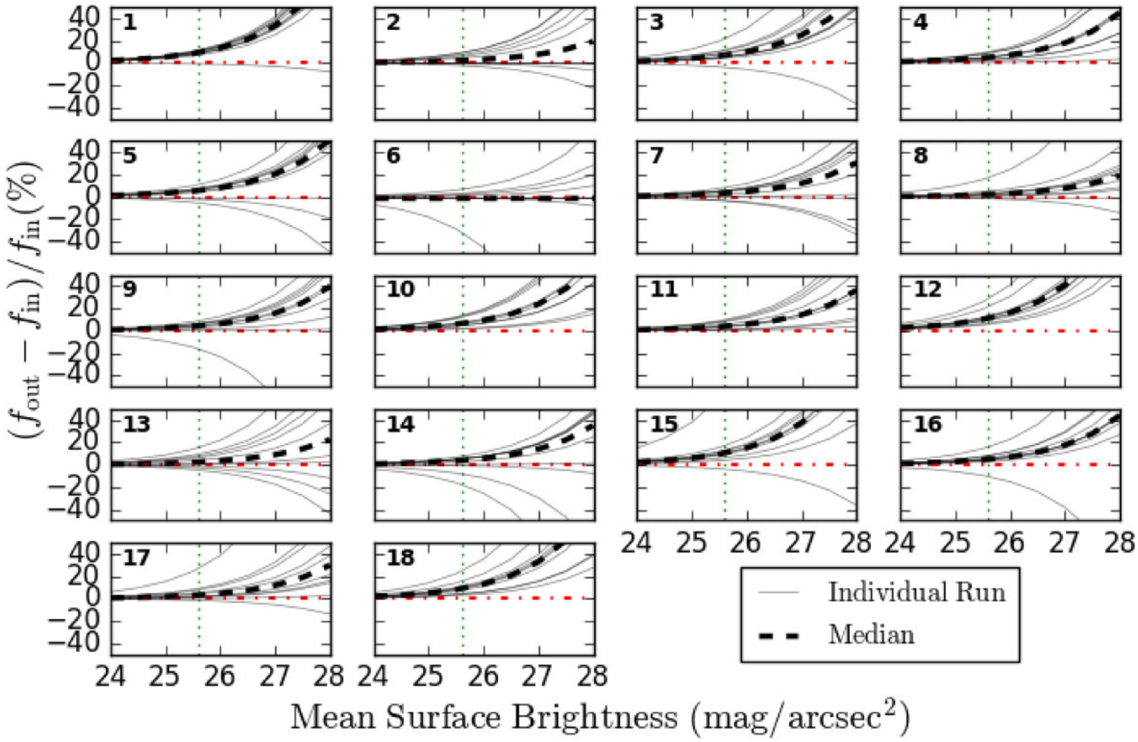

Figure 6. The results from performing photometry on ∼2000 mock ICL profiles injected into HSC data (without divot corrections; numerical labels have been included as in Fig. 5). Each frame in the subplot represents a given control field. The plot shows the relative percentage deviation in flux [$(f_{\rm out} - f_{\rm in})/f_{\rm in}$], where $f_{\rm in}$ is the raw mock profile flux measurement and $f_{\rm out}$ is the flux measurement of the profile after implantation in an HSC control frame for a given 'ICL-like' profile (see the text) with respect to mean surface brightness (the average surface brightness across a mock profile). The green dotted lines show the isophote of lowest surface brightness used in this work.

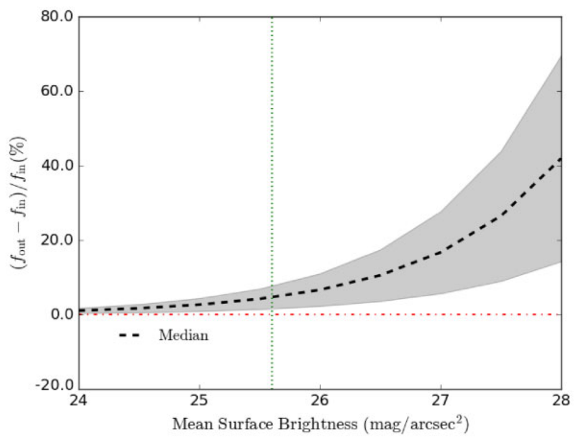

Figure 7. Stack of median deviations of recovered profiles across all frames with respect to mean surface brightness. The grey shaded region indicates the 1σ scatter. The green line shows the isophote of lowest surface brightness used in this work.

There is obvious scatter on a case-by-case basis (for example, panel 16 of Fig. 6; see also panel 16 of Fig. 5); from eyeballing, the predominant cause of this seems to be due to source-heavy frames (e.g. many/clustered sources or bright sources such as stars present). Moreover, we will show evidence in Section 6 that the flux lost through the divot effect at the range of isophotal levels at which we measure the ICL is approximately 4 × the background contribution; hence, we do not correct for it here (see further discussion of systematics in Section 5.5). It is again, however, worth noting that this method does not quantify the flux contribution of the population of faint galaxies below the survey limit (indeed, it is an issue with all similar observational studies of ICL, e.g. see Zhang et al. 2019).

5.5 Quantifying ICL

Observationally, past studies have generally taken two approaches when quantifying the amount of ICL present in a cluster: a parametric approach using model fitting (e.g. Gonzalez et al. 2005, 2007, 2013; Morishita et al. 2017), or by summing up the contribution of ICL below a set (usually isophotal) limit while masking out the BCG and any satellites (e.g. Krick & Bernstein 2005, 2007; Burke et al. 2012, 2015; Montes & Trujillo 2018). Other approaches looking at either the shape of the BCG+ICL profile (see upcoming discussion) or the so-called 'colour profile' (namely, how the colour of the ICL spatially varies across the cluster) have also measured the flux in isophotes or annuli to acquire a 1D profile (e.g. Burke et al. 2012; DeMaio et al. 2018; Zhang et al. 2019).

When modelling a profile, one must assume a prior; exactly the best model to use when describing the BCG+ICL profile varies enormously across studies, with some recommending a double de Vaucouleurs profile (e.g. Krick & Bernstein 2007), some using a Sérsic+Exponential (e.g. Lauer et al. 2007), and others more complicated models still (e.g. Zhang et al. 2019). Choosing the wrong profile can lead to large uncertainties (e.g. Zhao et al. 2015a); as well as this, the degeneracies present when using multiple component fits mean that one cannot readily disentangle individual flux contributions without dynamical information (e.g. Dolag et al. 2010). As per our masking methodology outlined in Section 5.3, we take an isophotal approach to measuring the ICL in our clusters,

Table 4. A summary of the results from this work, where $f_{\rm ICL}/f_{\rm tot}$ is the percentage of cluster light that is ICL at $\mu_{B,\rm rest} = 25$ mag arcsec^{-2} within $R_{\rm X,500}$ and Δf is the fractional difference in the ICL contribution between the divot-corrected and uncorrected cases. The equivalent BCG flux ($f_{\rm BCG}$) is also included (Sérsic model, de Vaucouleurs model, and 50 kpc aperture, respectively).

XCS ID	$f_{\rm ICL}/f_{\rm tot}$	Δf	$f_{\rm BCG}$ (Sérsic)	$f_{\rm BCG}$ (de Vaucouleurs)	$f_{\rm BCG}$ (50 kpc aperture)
XMMXCS J022456.1−050802.0	0.2896 ± 0.0009	0.0473 ± 0.0042	0.2829 ± 0.0007	0.2889 ± 0.0007	0.2653 ± 0.0013
XMMXCS J161039.2+540604.0	0.1877 ± 0.0099	0.0547 ± 0.0091	0.1631 ± 0.0033	0.1704 ± 0.0030	0.1382 ± 0.0010
XMMXCS J233137.8+000735.0	0.2628 ± 0.0010	0.0626 ± 0.0076	0.1731 ± 0.0009	0.1568 ± 0.0006	0.2469 ± 0.0025
XMMXCS J232923.6−004854.7	0.2757 ± 0.0009	0.0495 ± 0.0055	0.1560 ± 0.0011	0.1657 ± 0.0010	0.1201 ± 0.0008
XMMXCS J161134.1+541640.5	0.1540 ± 0.0006	0.0245 ± 0.0060	0.0901 ± 0.0004	0.0871 ± 0.0003	0.0690 ± 0.0007
XMMXCS J095902.7+025544.9	0.2676 ± 0.0012	0.0780 ± 0.0076	0.1178 ± 0.0006	0.1159 ± 0.0005	0.0895 ± 0.0008
XMMXCS J095901.2+024740.4	0.1148 ± 0.0017	0.0441 ± 0.0294	0.3442 ± 0.0159	0.1705 ± 0.0012	0.2058 ± 0.0028
XMMXCS J100141.6+022538.8	0.3121 ± 0.0007	0.0716 ± 0.0036	0.2563 ± 0.0005	0.2535 ± 0.0005	0.2254 ± 0.0013
XMMXCS J095737.1+023428.9	0.1567 ± 0.0007	0.0586 ± 0.0087	0.1244 ± 0.0010	0.1291 ± 0.0009	0.1535 ± 0.0012
XMMXCS J022156.8−054521.9	0.2887 ± 0.0012	0.0652 ± 0.0071	0.2261 ± 0.0026	0.1550 ± 0.0008	0.1269 ± 0.0010
XMMXCS J022148.1−034608.0	0.0972 ± 0.0008	0.0354 ± 0.0170	0.0670 ± 0.0012	0.0700 ± 0.0010	0.0561 ± 0.0004
XMMXCS J022530.8−041421.1	0.3843 ± 0.0008	0.0335 ± 0.0032	0.1660 ± 0.0007	0.1275 ± 0.0003	0.1506 ± 0.0009
XMMXCS J100047.3+013927.8	0.2385 ± 0.0006	0.0391 ± 0.0041	0.0859 ± 0.0004	0.0852 ± 0.0003	0.0850 ± 0.0007
XMMXCS J022726.5−043207.1	0.2971 ± 0.0009	0.0337 ± 0.0048	0.0551 ± 0.0002	0.0599 ± 0.0002	0.0869 ± 0.0006
XMMXCS J022524.8−044043.4	0.3276 ± 0.0012	0.0627 ± 0.0059	0.1302 ± 0.0008	0.1364 ± 0.0006	0.0977 ± 0.0008
XMMXCS J095951.2+014045.8	0.1985 ± 0.0012	0.0410 ± 0.0100	0.2792 ± 0.0018	0.2839 ± 0.0013	0.1895 ± 0.0016
XMMXCS J022401.9−050528.4	0.2762 ± 0.0024	0.0334 ± 0.0131	0.1860 ± 0.0014	0.1719 ± 0.0007	0.1503 ± 0.0015
XMMXCS J095924.7+014614.1	0.3078 ± 0.0008	0.0542 ± 0.0042	0.1170 ± 0.0003	0.1195 ± 0.0003	0.1342 ± 0.0012
Average	**0.2434 ± 0.0015**	**0.0475 ± 0.0085**	**0.1930 ± 0.0020**	**0.1799 ± 0.0001**	**0.1642 ± 0.0013**

which we do for two reasons: simplicity and to keep our assumptions minimal. While the approach of using a surface brightness limit is not perfect (and often leads, according to Rudick et al. 2011, to a lower ICL estimate), it is at least model independent. Here, we choose a limit of $\mu_B = 25$ mag arcsec^{-2} in the rest-frame B band, similar to Burke et al. (2015); we discuss our methodology in Section 5.3.

After applying a mask (which includes an isophotal threshold), we sum the weighted flux within an aperture of $R_{\rm X,500}$ centred on the cluster BCG and repeat the process without an isophotal limit (Section 5.3). We also provide comparisons at the equivalent surface brightness levels of 24 and 26 mag arcsec^{-2}, respectively, to assess the effect of changing the selected surface brightness on the recovered ICL. The ICL measurement errors, E(ICL), are computed directly from the image variances as follows:

$$E(\mathrm{ICL}) = \sqrt{\left(\frac{\sigma_{\rm ICL}}{f_{\rm tot}}\right)^2 + \left(\frac{f_{\rm ICL} \times \sigma_{\rm tot}}{f_{\rm tot}^2}\right)^2}, \tag{8}$$

where the subscripts ‘ICL’ and ‘tot’ refer to the ICL and total flux, respectively, f is the flux in counts, and σ denotes the standard deviation.

6 RESULTS

6.1 How much of a cluster is ICL?

For comparison, we measure the ICL for our clusters before and after applying a divot correction. The measurements are summarized in Table 4. In Section 6.2, we will provide more extensive comments on our results and their consequences for BCG evolution; here, we restrict our commentary towards the inferred *systematics* involved in ICL measurement for ease of comprehension.

For our clusters, with the inclusion of a divot correction, the mean ICL contribution to the total cluster light at $\mu_{B,\rm rest} = 25$ mag arcsec^{-2} sits at around 24 per cent. It is immediately clear from Table 4 that applying a divot correction has a significant effect on the overall recovered value for the ICL (Δf being the difference in ICL to total

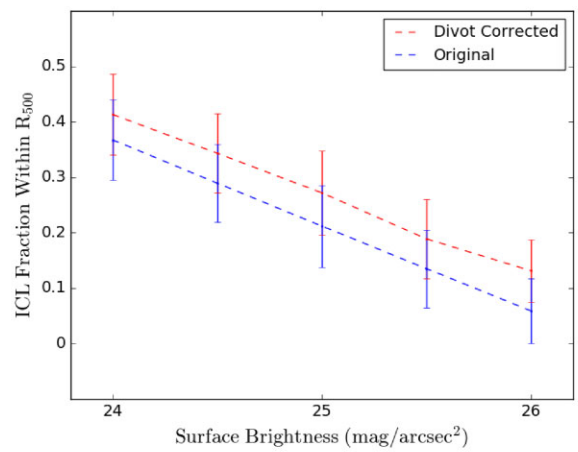

Figure 8. The stacked ICL fraction at a selection of equivalent surface brightnesses, comparing the divot-corrected and uncorrected cases. The errorbars depict the 1σ scatter across all clusters in the sample.

cluster light between the divot-corrected and uncorrected values); Fig. 8 illustrates this difference, for equivalent surface brightness limits in B from 24 to 26 mag arcsec^{-2} in steps of 0.5 (as a side note, we used these measurements to estimate the choice of stellar population model on the final ICL fraction, as discussed in Section 5.3). On average, the ICL fraction is ∼5 per cent higher with a divot correction included, which represents ∼20 per cent of the mean measured ICL light fraction overall. The final masked, divot-corrected images are shown in Fig. 5.

Our results illustrate exactly how crucial it is to account for the flux oversubtraction problem around objects in surveys. As stated previously, because the divot corrections are modelled with a ‘one-size-fits-all’ Sérsic profile, it is likely that the ‘true’ net flux loss is underestimated due to our choice of Sérsic profile with which to model our divot corrections, with ∼50 per cent of BCGs tending to have an additional ‘halo’ as well as a central bulge by $z <$

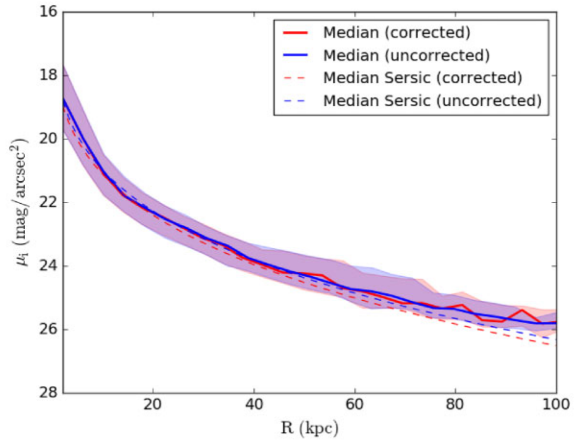

Figure 9. Comparison between the divot-corrected and uncorrected stacks as measured by IRAF ellipse. The shaded region represents the 16th and 84th percentiles of the stacks, and the solid lines are the respective medians. The dashed lines are the median Sérsic model from SIGMA in each respective case. Although not very pronounced here, the Sérsic models appear to miss some flux on the outskirts of the BCGs, which previous authors have argued is a plateau of either ICL or a cD halo. There is little difference in the median n values, with values of 4.65 and 4.57 for the non-corrected and corrected models, respectively.

0.1 that is debated to be either ICL or a BCG component (Zhao et al. 2015a). In addition, our method, as for other observational methods for measuring ICL that utilize a surface brightness limit, clearly cannot account for ICL in projection of the BCG. While we appreciate that there is a method dependence when measuring ICL, there is still a significant difference upon inclusion of a divot correction when changing the surface brightness limit (Fig. 8).

As a sanity check, to measure the BCG+ICL profile shape, we fit elliptical isophotes using the IRAF ELLIPSE package (Jedrzejewski 1987) centred on each cluster BCG, for both the pre- and post-divot-corrected images. The frames are masked at $\mu_{B,\mathrm{rest}} = 24$ mag arcsec^{-2} using the segmentation maps from SEXTRACTOR (plus all-star/bad pixel masks), due to the convenience of the software having an inbuilt de-blending algorithm to separate object fluxes (with the exception of the BCG itself, which is left unmasked during this process). A stack of the resulting profiles is shown in Fig. 9. Interestingly, we do not find much deviation in shape on average when applying a divot correction within the percentiles of the stacks, which supports the comparable outputs we obtained through our SIGMA models.

Our results illustrate that one must consider their data carefully when attempting to measure ICL. Indeed, many authors have recognized this issue and have attempted to overcome it by using novel processing methods of their own, such as implementing less 'aggressive' global background subtraction techniques (often, for example, using a larger mesh, e.g. Huang et al. 2018a, or a mean global 'step', e.g. Montes & Trujillo 2019).

We recognize that there are several obvious caveats with our method; as aforementioned, surface brightness methods of measuring ICL tend to recover less flux than methods more readily available in simulations such as setting a binding energy threshold (e.g. Rudick et al. 2011). We also assume the location of the BCG to be a proxy for the centre of the cluster when measuring the ICL. For local systems, this is often the case (e.g. Lin & Mohr 2004); however, the picture has been known to change at high redshift, with higher number of clusters out of dynamical relaxation at $z > 1$ (e.g. Hatch et al. 2011). Having outlined these caveats, we proceed with the view that we have utilized a method that relies as little as possible on parametric modelling; we refer the reader towards arguments for our approach in Section 5.5 of this paper.

Table 5. Full Spearman analysis of all the parameters used in this study: the fractional contribution of the ICL and of the BCG ($f_{\mathrm{ICL}}/f_{\mathrm{tot}}$ and $f_{\mathrm{BCG}}/f_{\mathrm{tot}}$, respectively), the cluster redshift (z), and the cluster mass $M_{\mathrm{X},500}$. The top half of the table lists the Spearman rank correlation coefficient (r_s), whereas the bottom half of the table provides the log of its corresponding p-value ($\log_{10}[p_s]$, expressed as such due to some p-values being very small).

	$f_{\mathrm{ICL}}/f_{\mathrm{tot}}$	$f_{\mathrm{BCG}}/f_{\mathrm{tot}}$	z	$\log_{10}M_{\mathrm{X},500}$
$f_{\mathrm{ICL}}/f_{\mathrm{tot}}$	–	0.0807	− 0.7860	− 0.2070
$f_{\mathrm{BCG}}/f_{\mathrm{tot}}$	− 0.1292	–	− 0.1526	− 0.7474
z	− 4.0174	− 0.2746	–	0.3561
$\log_{10}M_{\mathrm{X},500}$	− 0.4051	− 3.4491	− 0.8700	–

6.2 What drives ICL growth?

To enable a more complete interpretation of our results, we perform a partial Spearman analysis on our sample of 18 clusters (see Furnell et al. 2018, for method). The partial Spearman enables us to account statistically for underlying correlations that may be present through the means that we have selected our clusters. Here, we choose four primary parameters of interest: the fractional contribution of the ICL and of the BCG ($f_{\mathrm{ICL}}/f_{\mathrm{tot}}$ and $f_{\mathrm{BCG}}/f_{\mathrm{tot}}$, respectively), the cluster redshift (z), and the cluster mass $M_{\mathrm{X},500}$ (which is computed from the X-ray temperature, as detailed in Section 2). We also look at correlations between k-corrected BCG absolute magnitude, cluster mass, and redshift via a similar means. We hold our significance at the standard value of $p \leq 0.05$ throughout ($\log_{10}[p_s] \leq -1.301$). The full Spearman analysis for our clusters is given in Table 5; the partial analysis can be found in Appendix B (Tables B1–B4).

As aforementioned, in the rest-frame B band, we find a mean ICL flux fraction of around 24 per cent; this exceeds the mean BCG contribution, even when using a Sérsic model (16–19 per cent; see Table 4). Qualitatively, however, the difference between the BCG and ICL flux contributions appears to decrease with redshift, with a less than 1 per cent difference for 2/4 of the most distant systems (with XMMXCS J022148.1−034608.0 being the exception at ∼4 per cent) and a reversal of the trend for the highest redshift system at $z = 0.501$. This is not a definitive conclusion, in that we are obviously limited by our small sample size (18 systems) as is the case for most legacy studies of ICL (see references in the Introduction), alongside significant caveats with assuming a fixed aperture scale when measuring the fluxes of our BCGs. However, it raises interesting questions as to what point in time the ICL begins to dominate the cluster halo (see Section 6.3).

In common with other authors (e.g. Burke et al. 2015, and upcoming discussion), we detect a significant anticorrelation ($r_s = -0.786$, $\log_{10}[p_s] = -4.017$) between the contribution of ICL with cluster redshift, which remains almost entirely unchanged when fixing for cluster mass (see Table B4 in the appendix). This is clearly visible in Figs 15 and 16, which we will discuss in Section 6.3. This is not the case for the BCG flux fraction, which has no significant correlation with redshift ($r_s = -0.153$, $\log_{10}[p_s] = -0.275$; see Fig. 11) and remains highly anticorrelated with the cluster mass even after fixing for redshift ($r_s = -0.750$, $\log_{10}[p_s] = -3.477$; see Table B3 in the appendix and Fig. 10). Even if we consider a Sérsic model (which produces almost universally the largest BCG fraction estimates) in place of an aperture magnitude for our BCGs, there is still an anticorrelation present at fixed redshift that remains almost

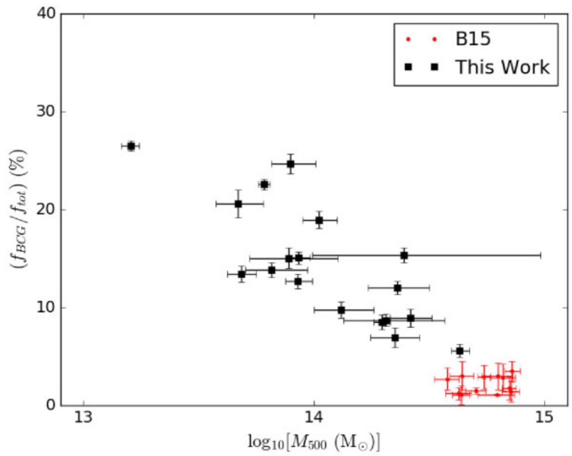

Figure 10. Plot of the BCG to total flux contribution (within a 50 kpc aperture) with respect to halo mass, $M_{X,500}$. The BCG flux contributions from Burke et al. (2015) (B15) have been plotted for comparison, which we discuss further in Section 6.3. It is clear that there is a strong anticorrelation with halo mass (see the text).

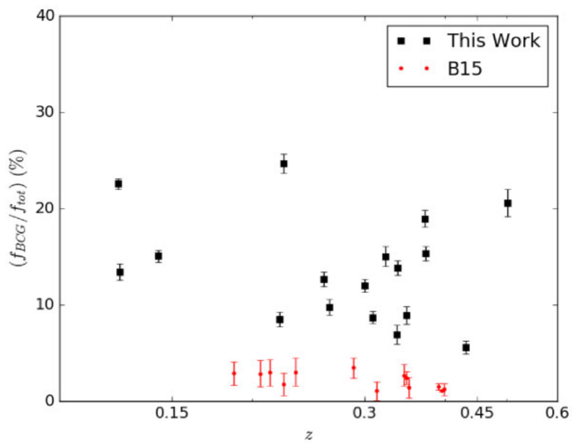

Figure 11. Plot of the BCG to total flux contribution (within a 50 kpc aperture) with respect to redshift, z. The BCG flux contributions from Burke et al. (2015) (B15) have been plotted for comparison. As shown in the partial Spearman analysis, there is no clear trend with redshift.

unchanged ($r_s = -0.775$, $\log_{10}[p_s] = -3.801$), so the trend is robust to the flux loss through not accounting for galaxy profile wings.

There is no strong correlation present, however, between the ICL and the mass of the cluster at fixed redshift ($r_s = 0.126$, $\log_{10}[p_s] =$ from Table B3). This has an interesting implication, in that our findings imply a much closer dependence between stars within the very central region of the halo (BCG) with the halo properties (such as M_{500}) in comparison to stellar mass distributed further out (ICL). Indeed, with a lack of correlation present between halo mass and ICL mass, there seems to be a 'decoupling' between the two components; the ICL, for instance, has been found to exhibit far more growth since $z \sim 1$ than the BCG (e.g. Burke et al. 2012, 2015), with BCG growth rates being much more modest than those generally predicted from simulations.

The leftmost panel of Fig. 12 shows the relationship between the k-corrected BCG absolute magnitude (M_i, i-band aperture; see Section 6.3) and cluster mass ($M_{X,500}$). Although we detect an anticorrelation between halo mass and absolute magnitude (which is anticorrelated with BCG mass), it is not significant ($r_s = -0.408\,77$, $\log_{10}[p_s] = -1.0785$). This finding is also the case if we fix for redshift ($r_s = -0.274\,56$, $\log_{10}[p_s] = -0.568\,31$). If we remove the two points with the largest errorbars, it becomes significant by our criteria, but still remains insignificant with fixed redshift ($r_s = -0.487\,75$, $\log_{10}[p_s] = -1.3094$; $r_s = -0.371\,36$, $\log_{10}[p_s] = -0.804\,87$, respectively). We therefore do not find conclusive evidence that our BCG absolute magnitudes (and therefore masses) are strongly governed by halo mass here. This is likely to be as a result of our selection (e.g. Burke et al. 2015) and also due to the fact that our sample size is small. An obvious point would therefore be to establish whether our result for the BCG flux fraction with halo mass weakens when applying our method to a larger sample of clusters with an established M_{BCG}–M_{halo} relation; this was also recognized in Burke et al. (2015).

We find a similar result for absolute magnitude with redshift when fixing for halo mass ($r_s = -0.460\,34$, $\log_{10}[p_s] = -1.2632$; see the rightmost panel of Fig. 12) even having removed the two points with the largest error bars ($r_s = -0.314\,43$, $\log_{10}[p_s] = -0.627\,85$); hence, we do not detect any significant change in BCG brightness with redshift either. Although this may also be linked to the way we have selected our BCGs, given numerous authors have found little change in BCG brightnesses since $z \sim 1$ (e.g. Whiley et al. 2008; Collins et al. 2009; Stott et al. 2010), our result acts to support trends found by other works using independent data sets.

6.3 Comparison with other studies

We show the results from a number of other studies of ICL, from both simulations and observations, in Figs 13–16 alongside our results. Where relevant, we have included descriptions giving context to the results presented in the plots. The shorthand for the observational studies shown in the legends of the plots is as follows: Gonzalez et al. (2013) (G13, parametric model) and Burke et al. (2015) (B15, $\mu_B = 25$ mag arcsec^{-2}). Respectively, the shorthand for the simulation-based studies presented in the legends of the plots is as follows: Puchwein et al. (2010) [P10, both with and without an active galactic nucleus (AGN) feedback prescription applied], Rudick et al. (2011) (R11, $\mu_V = 25$ mag arcsec^{-2}), Contini et al. (2014) (C14, disruption model only), and Tang et al. (2018) (T18, $\mu_V = 24.7$ mag arcsec^{-2}, mock SDSS r band; closest to our own data). All observational masses have been scaled from X-ray measurements (from either *XMM–Newton* or *Chandra* in the case of the majority of the CLASH clusters) using the same scaling relation (Arnaud et al. 2005). In the case of the CLASH sample, it is worth noting that clusters with $T > 5$ keV have an ~15 per cent mass increase on average between values computed from *Chandra* versus *XMM–Newton* data (see discussion in DeMaio et al. 2018 and Mahdavi et al. 2013); however, scaling the points does little to influence the interpretation of our comparisons (see upcoming discussion). In the case of the theoretical studies, the density contrast was scaled where necessary (e.g. from $\rho_c = 200$ to 500) using the method outlined in Hu & Kravtsov (2003), assuming an Navarro-Frenk-White (NFW, see Navarro, Frenk & White 1996) profile with a concentration of 3.

Figs 13 and 14 show the relationship between the BCG+ICL fraction and the ICL fraction with cluster mass, respectively. In both cases, there is an obvious difference between the results from simulations and observations, in that while the observations qualitatively appear fairly consistent (see upcoming discussion) the simulations appear to predict significantly larger BCG+ICL (or ICL) contributions to the overall cluster light. The exception here is Contini et al. (2014), whose results are consistent with observations (Fig. 14); their

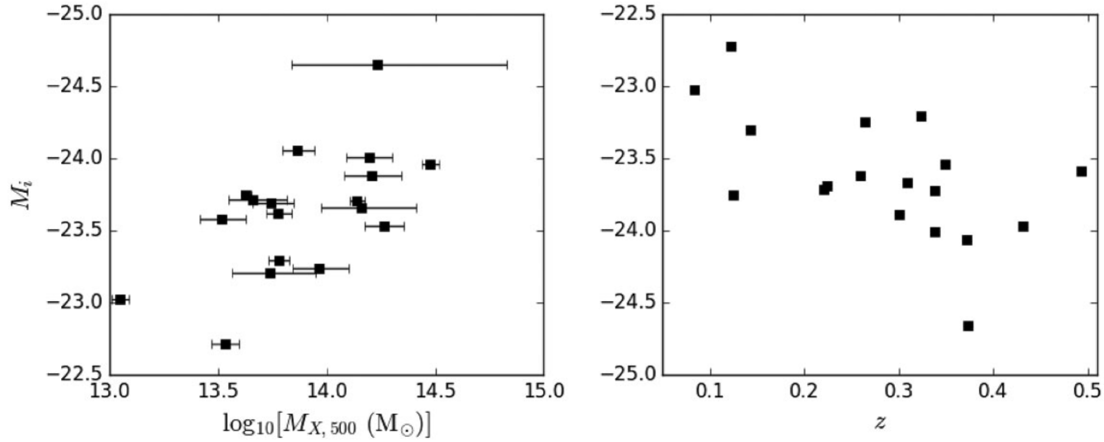

Figure 12. The rest-frame BCG absolute magnitude (M_i, i-band aperture) versus cluster mass measured in X-rays ($M_{\mathrm{X},500}$, left) and redshift (z, left). For ease of comprehension, we have inverted the y-axis. No significant trends are detected in our partial Spearman analysis between BCG magnitudes with either redshift or halo mass.

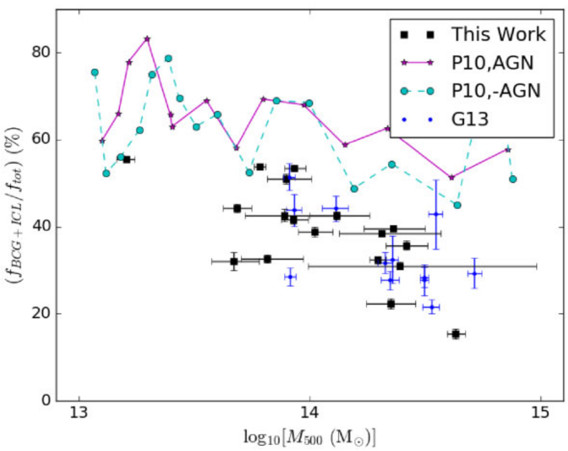

Figure 13. Comparison of the relative fluxes of ICL+BCG versus halo mass. The legend key is as follows: Puchwein et al. (2010) (simulation) with/without an AGN prescription (P10, AGN/-AGN) and Gonzalez et al. (2013) (G13, observational). It is clear that P10 does not agree with either our observational results or the results of G13.

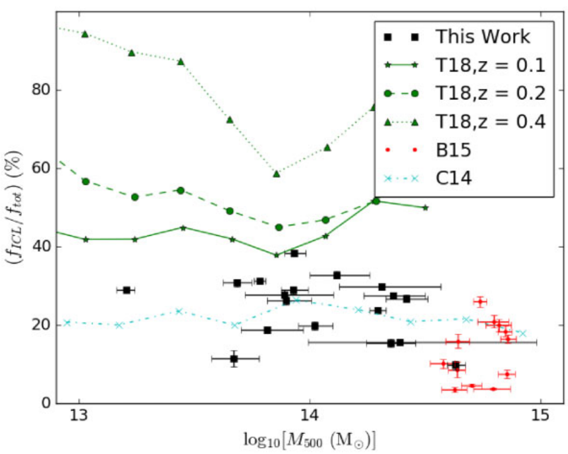

Figure 14. As in Fig. 13, but for ICL flux only (see the text). The legend key is as follows: Tang et al. (2018) at redshift z (T18, simulation), Burke et al. (2015) (B15, observational), and Contini et al. (2014) (C14, simulation). With the exception of C14, there is a clear disagreement between the observations and simulations.

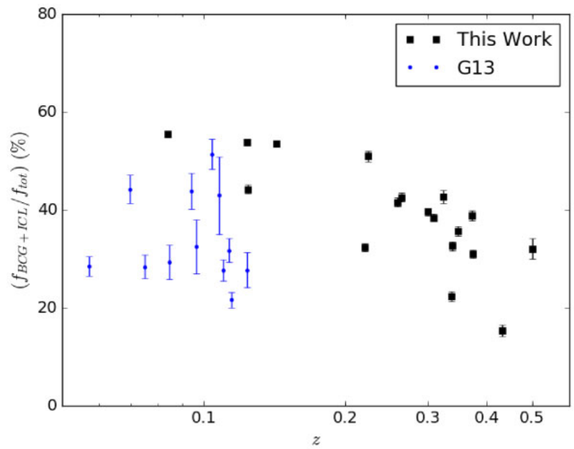

Figure 15. Comparison of the relative fluxes of ICL+BCG versus redshift, with the points from Gonzalez et al. (2013) (G13).

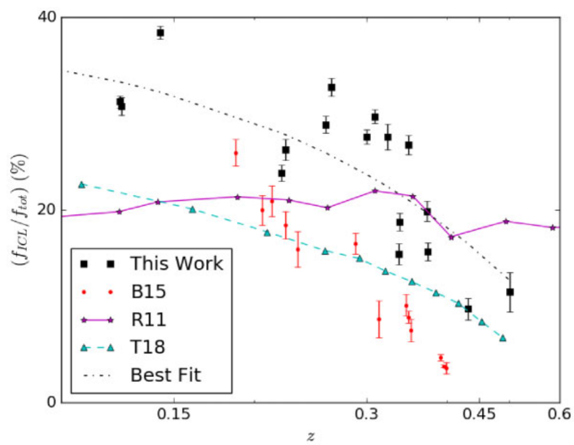

Figure 16. As in Fig. 15, but only for ICL flux. The legend key is as follows: Burke et al. (2015) (B15), Rudick et al. (2011) (R11), and Tang et al. (2018) (T18). The best least-squares fit has been included for comparison (slope = −54.50, intercept = +40.01).

simulations are, however, semi-analytic rather than hydrodynamic. Although not plotted here, larger BCG+ICL fractions than those seen observationally (60–80 per cent compared with 1–60 per cent) were also found by Cui et al. (2014), who, using hydrodynamical simulations (for specifics, see Bonafede et al. 2011), measured the BCG+ICL light using a *V*-band surface brightness limit, similar to our own approach. Contini et al. (2014) also found that their ICL fractions were also very sensitive to AGN and supernova feedback; this is in contrast to Puchwein et al. (2010), as while the BCG+ICL fractions themselves are similar, there was little difference found between the fractions detected when an AGN model was used (see Fig. 13). An exception using simulations is Murante et al. (2007), who found a much lower average fraction of ICL with respect to halo mass (∼22 per cent) in a similar mass range to that of the CLASH clusters (10^{14}–$10^{15}\,\mathrm{M}_{\odot}$); however, they found a positive correlation between halo mass and the fraction of ICL, which has not been seen observationally. In fact, the opposite has increasingly been reported, with lower mass haloes found to be more 'efficient' producers of stellar mass than large clusters (e.g. fig. 8 of Tang et al. 2018, simulations; DeMaio et al. 2018 and Erfanianfar et al. 2019, both observations).

Results for the ICL light fraction with respect to the overall cluster from numerical simulations and SAMs appear generally to be more self-consistent than those obtained observationally (e.g. for our work, 20–40 per cent; see Contini et al. 2014; Rudick et al. 2011, for some typical SAM results). Barai, Brito & Martel (2009), using a numerical prescription, simulated the build-up of intracluster stars using several different cluster mass profiles (e.g. Perseus-like to Virgo-like) while considering the morphology of the galaxies contained within the cluster (e.g. if the BCG was a cD-type). They found mean ICL fractions of ∼25 per cent for a Virgo- or Perseus-like system, compared with much higher fractions (∼40 per cent) for an NFW model; they also found a dependence of the ICL fraction on the morphology of the BCG (with cD-type BCGs leading to generally more centrally concentrated ICL profiles). Henriques & Thomas (2010), building on the semi-analytic study of BCG mass growth of De Lucia & Blaizot (2007), included a prescription for ICL (tidal disruption and dynamical friction); they found a mean fraction of ICL of around 18 per cent, with a positive correlation between the ICL fraction and the halo mass of the cluster. Contini et al. (2014) used dark matter haloes from the Millennium Simulation, coupled with several simple dynamical models (e.g. mergers, disruption, and tidal stripping), finding results similar to observations in Gonzalez et al. (2013) (and indeed, our own), with no correlation with halo mass.

Here, we detect no strong trend between halo mass and the fraction of ICL (as is the case in Burke et al. 2015); it is therefore possible that any gradients present in Fig. 13 are driven by the strong anticorrelation between the BCG flux fraction and halo mass established in Section 6, as they are not present with the ICL fraction itself. Toledo et al. (2011) also find little evidence dynamically for any strong relation between the BCG+ICL fraction with cluster mass for a single cluster at $z \sim 0.3$, acquiring a total fraction of ∼70 per cent in line with the low-z ($z < 0.1$) results of Gonzalez et al. (2007), though higher than the latter's 2013 revisited study (Gonzalez et al. 2013; see Figs 13–15) and indeed, our own work. Our results with respect to halo mass are fairly consistent observationally with the other studies presented in Figs 13 and 14, with the ∼24 per cent ICL fraction and ∼41 per cent BCG+ICL fraction seen here comparable with the respective results of Burke et al. (2015) and Gonzalez et al. (2013). As discussed at length, however, in the Introduction, observational results for ICL dramatically vary in general, with a dependence on the data used and the measurement approach (see fig. 8 of Tang et al. 2018).

Tang et al. (2018) investigated the limitations of measuring ICL from optical imaging data using hydrodynamical simulations. Although their ICL result differs significantly from our own and that of Burke et al. (2015), their findings on the causes of what effects drive scatter in ICL measurements are arguably far more interesting. Using simulated images of their clusters, they produced mock images with numerous observational differences, such as band, pixel size, surface brightness limit, and PSF size. They found a clear effect from the PSF, finding that large PSFs lead to greater smoothing and a slightly higher ICL fraction (5–10 per cent; see upcoming discussion). They also found a band dependence on the ICL fraction, finding that the *r* band yielded a much larger ICL fraction (∼2×) even when using the same equivalent *V*-band surface brightness limit; they attribute this in their discussion to uncertainties in their stellar population model of choice (Bruzual & Charlot 2003, with a Chabrier 2003 IMF). They also found that the surface brightness limit also affected their ICL result, finding a doubling in the amount of ICL detected between $23.0 < \mu_V < 26.5$ for low-redshift haloes (also observed in Cui et al. 2014, from whom their method for generating mock images was derived). Finally, Tang et al. (2018) also found a clear dependence of cosmological dimming on their ICL, finding an *increase* in the relative fraction of ICL up to $z \sim 1$ when accounting for surface brightness dimming (see the rightmost panel of their fig. 6). Their results suggest a clear motivation for more studies of this kind, as such a result has unexpected consequences regarding the current widely accepted paradigm of BCG–ICL co-evolution (see Introduction), given it is canonically thought that the period $0 < z < 1$ is an era of rapid ICL growth, with little changes in the luminosity of the BCG.

The theoretical studies presented here also obviously differ enormously in their methodology, with some using methods to estimate ICL that are not observationally feasible (such as tracking star particles). It is, however, curious that despite more complex physical models being included in hydrodynamical simulations, they generally seem to struggle to reproduce ICL fractions with cluster mass in contrast to either a simple numerical or semi-analytic prescription. This therefore presents a challenge to these modern simulation suites and an opportunity for further analysis to better understand the reasons behind these differences, such as the effects of subgrid size and the physical models used. Future studies resembling this work with larger cluster samples (e.g. in the wake of the Vera C. Rubin Observatory) will also help in our understanding of these discrepancies.

Figs 15 and 16 show the trend of our results with redshift, for the BCG+ICL fraction and ICL fraction, respectively. Although we appear consistent with Gonzalez et al. (2013) in Fig. 15, there is some deviation present between our results and those presented in Fig. 16 (e.g. Burke et al. 2015), in that our fractions with redshift appear noticeably higher. Interestingly, however, there seems to be no clear consensus overall, with the slopes of ICL growth differing clearly across studies. There may be several reasons as to why this may be the case. First, as noted in Tang et al. (2018), observational results are strongly influenced by several factors. The PSF, for example, was found by Tang et al. (2018) to produce a scatter of 5–10 per cent in the total ICL fraction at a redshift range similar to that explored here ($0 < z < 0.4$ from their fig. 3, $\mu_V = 26.5$), with a smaller PSF (such as those found using space-based observatories as in CLASH) and usually also produced smaller results for the ICL fraction. They also found that measuring the ICL in a redder passband (SDSS *r*) increased the fraction of ICL detected, even when using the same equivalent threshold, by around a factor of 2.

The results from Tang et al. (2018) presented in Fig. 16 represent an SDSS-like, *V*-band image with the ICL measured using an isophote of $\mu_V = 24\,\mathrm{mag\ arcsec}^{-2}$, with cosmological surface brightness dimming not being taken into account. This corresponds to a growth factor of $\sim$3, similar to what we observe. As previously mentioned, Tang et al. (2018) do not actually find any physical growth of the ICL over cosmic time; in fact, they find the ICL contribution to dramatically shrink with decreasing redshift. This result sets them starkly apart from most other theoretical studies, which, within the redshift range explored in this work, find fractional increases in the ICL relatively consistent with our own of 1.5–4 (e.g. Willman et al. 2004; Murante et al. 2007; Rudick et al. 2011; Contini et al. 2014).

Some of the observational reasons outlined in Tang et al. (2018) may partially account for the difference we see between our results and the results of Burke et al. (2015). We have, for example, larger k-corrections due to our use of a redder band (HSC-i); testing EZGAL using the bands used in CLASH (F606W, F626, F775, and F850LP) with an identical stellar evolution model, however, produced similar results to Burke et al. (2015), with the same trends. Our data are also ground based with a larger PSF ($<$FWHM$>$ $\sim$0.56 arcsec for HSC; see Aihara et al. 2018b), which we correct for when fitting profiles (but we do not deconvolve our data when computing ICL); the effect of this on recovering the magnitudes in the HSC-SSP-Wide data was investigated in detail by Huang et al. (2018a), where they determined a 10–18 per cent margin of error in i-band magnitudes at 25th mag (see also Huang et al. 2018b). HSC-SSP-Deep is $\sim$1 mag deeper than that of CLASH (where, as noted in Burke et al. 2015, a difference in 0.5 mag in survey depth results in a 5–10 per cent reduction in the amount of measured ICL component). Our values are, of course, also divot corrected.

One of the biggest differences we observe is that of the fractional contribution of the BCG, in that ours are far larger than those stated in Burke et al. (2015) ($\sim$19 per cent compared to $\sim$5 per cent; see Fig. 12). It is not clear from Burke et al. (2015) whether the fractions are measured relative to a set absolute cluster radius (here, $R_{\rm X,500}$ in kpc); however, using a radius of R_{500}, similar low BCG fractions are seen in Burke et al. (2012) (2–4 per cent depending on whether a de Vaucouleurs model or 50 kpc aperture is used). This differs significantly from numerous other works, with which our BCG fractional contribution to the overall cluster light is more consistent; it is, for example, comparable to Zibetti et al. (2005) at $z \sim 0.25$, who fit de Vaucouleurs profiles and measure the relative fractions contained within a fixed radius of 500 kpc centred on the BCG. A BCG stellar mass contribution to the overall halo of around 15–40 per cent was also noted by Shan, McDonald & Courteau (2015), as well as in Seigar et al. (2007). The CLASH sample constitutes especially massive systems, with the range of cluster masses representing the larger end of the cluster population ($\sim$10^{15} M$_\odot$); no overlap is present with our sample. As other authors have shown (e.g. Andreon 2010; Erfanianfar et al. 2019), there appears to be an increasing inefficiency in stellar mass production with increasing halo mass, particularly with respect to the BCG.

There is also the added issue of how CLASH data were optimized for science, in that its original focus was specifically to study the lensed and high-z Universe, rather than LSB science (Postman et al. 2012). The background subtraction method is therefore generally more aggressive than ideal (although there is a focus on lensing in HSC, there is also an LSB science focus and a great deal of pipeline refinement in preparation for the Vera C. Rubin Observatory). In addition, *HST*'s ACS has a far smaller field of view ($\sim$3.36 arcmin) than HSC ($\sim$1.5°), as well as a very small associated dither pattern in CLASH. The majority of the clusters within CLASH (given their redshift) therefore would fill the majority of a frame (for example, a cluster with a radius of 0.7 Mpc at $z = 0.4$ has an angular extent of 2.2 arcmin, assuming our concordance cosmology). This implies that it is unlikely that the true background is reached (i.e. that there is little available sky with respect to source), leading to an overestimate of the background. As a further example, the 'missing flux' issue with the *HST* WFC3 (which has a smaller FOV than the ACS at 2.7 arcmin) data was explored in detail in Borlaff et al. (2019), who produced a pipeline to re-reduce the *Hubble* Ultra-Deep Field data (Beckwith et al. 2006); they found, when re-reduced, an integrated magnitude of recovered light of $\sim$20 mag, which they state is comparable to the brightest galaxies in the field. Although Borlaff et al. (2019) did not apply their method to the CLASH data, it is likely, given the comparable observational and data-reduction methodology, that it suffers from the same issue. This issue in particular may well be a large factor in the difference between the results of Burke et al. (2015) and our own. With its larger FOV, HSC SSP DR1 is more appropriate for LSB science (see, for example, fig. 5 of Aihara et al. 2018b); moreover, further pipeline processing improvements have been made with the release of DR2 (see, for example, discussions in Aihara et al. 2019). Work is currently underway to establish how effective the DR2 pipeline will be for the deeper data stream from the Vera C. Rubin Observatory (e.g. Watkins et al., in prep.).

7 SUMMARY AND CONCLUSIONS

In this work, we measured the ICL in 18 XCS-HSC clusters alongside consideration of two systematics: background contribution and sky oversubtraction. We discussed the sample of clusters in XCS used in this work and how they were selected; we also discussed the HSC-SSP survey, the current processing pipeline, and the photometry used. We outlined how we measured our ICL, using an equivalent B-band isophotal threshold, measured within an aperture of radius $R_{\rm X,500}$ centred on the BCG. We introduced the 'divot' problem, which arises due to an 'oversubtraction' of flux from background estimation during image processing, and our method to correct for this effect. Finally, we introduced a set of basic simulations to allow us to understand the flux contribution from the background at a given mean surface brightness for an ICL-like profile.

We then presented our results alongside numerous other studies for comparison, from simulations and observations. We noted a large degree of scatter, observationally (1–60 per cent globally, 20–40 per cent for our sample) and theoretically (10–90 per cent) for retrieved ICL fractions. We then discussed at length some of the reasons as to why such discrepancies may exist, such as the data used, the measurement methodology, the simulation method, and so on. Our primary conclusions are as follows:

(i) There is a loss in ICL flux of about 4 $\times$ the estimated background from the effects of sky oversubtraction, which remains approximately constant $\pm$1 mag arcsec^{-2} about our lowest chosen threshold. We surmised that this was likely to be an underestimate, given the Sérsic models used when creating the divot corrections.

(ii) The divot corrections themselves do little to change the overall profile shape, with the 1D profiles and parametric fits from SIGMA, respectively, yielding very similar results.

(iii) We detect no significant correlation between BCG absolute magnitude and redshift when fixing for halo mass. We also find the fractional contribution of BCG light with respect to the overall cluster light to be strongly anticorrelated with halo mass, inferring that star formation efficiency is inversely proportional to halo mass (e.g. Erfanianfar et al. 2019).

(iv) We find no strong evidence that the contribution of ICL to the overall stellar content of the cluster is strongly linked to halo mass, in line with most recent simulations.

(v) The fraction of ICL light is not strongly linked to the fractional contribution of the BCG (Section 6), indicating a 'decoupling' between the two components (e.g. DeMaio et al. 2018).

(vi) While finding generally higher fractions with redshift, we find the ICL to grow by a factor of ∼2–4 between $0.1 < z < 0.5$, slightly more modest than the factor of 4–5 in clusters over a similar range in redshift from Burke et al. (2015) albeit with a higher scatter ($rms\, f_{\rm ICL}/f_{\rm tot} \sim 10$ per cent).

(vii) We find a significant difference generally between hydrodynamical stellar mass fractions of ICL and BCG+ICL in clusters at a given halo mass, with the simulations almost always overpredicting the contribution (even when measured in an observationally consistent way). Numerical and SAM-based simulations, however, yield results closer to our observations.

Our work supports the current scenario of relatively rapid ICL build-up since $z \sim 0.5$, with BCGs remaining relatively unchanged with respect to absolute magnitude. There are also, as has been the case for most observational studies, discrepancies present between simulations. From the evidence presented here, it seems that a far greater understanding of the observational effects involved is needed (e.g. surface brightness limit used, band used, whether a BCG+ICL model fit is used, and PSF size), given that such effects, as noted in Tang et al. (2018), can change the ICL result obtained by a factor of 2.

As sample sizes grow larger and publicly available image data improve in depth with the new generation of telescopes in the coming decade (such as the Vera C. Rubin Observatory, which promises frequent periodic imaging of the whole southern sky coupled with an enormous FOV of $9.62\,\deg^2$; see Ivezic et al. 2008 and Brough et al. 2020), studies will be more readily able to untangle the degeneracies, e.g. between a detection of ICL growth and the effect of surface brightness dimming. For now, however, our results support the paradigm of ICL growth being the dominant stellar evolutionary component in galaxy clusters since $z \sim 1$.

ACKNOWLEDGEMENTS

We would like to thank the referee for their detailed comments that much improved and clarified this paper. KEF would like to thank the XCS team for their cooperation, collaboration, and support throughout this work. KEF would also like to thank L. S. Kelvin for his consistent advice, support, and for enabling the use of the SIGMA software. Finally, KEF would like to thank P. Bradshaw for providing unwavering support, kindness, and encouragement throughout her PhD. KEF is supported by a Science and Technologies Funding Council (STFC) award. CAC, IKB, and LSK are supported by an STFC research grant (ST/M000966/1). PTPV was supported by Fundaçõ para a Ciência e a Tecnologia (FCT) through research grants UIDB/04434/2020 and UIDP/04434/2020.

DATA AVAILABILITY

The data underlying this article will be shared on reasonable request to the corresponding authors via the email addresses provided.

REFERENCES

Abell G. O., 1958, ApJS, 3, 211
Aihara H. et al., 2018a, PASJ, 70, S4
Aihara H. et al., 2018b, PASJ, 70, S8
Aihara H. et al., 2019, PASJ, 71, 114
Albareti F. D. et al., 2017, ApJS, 233, 25
Andreon S., 2010, MNRAS, 407, 263
Arnaud M., Pointecouteau E., Pratt G. W., 2005, A&A, 441, 893
Barai P., Brito W., Martel H., 2009, J. Astrophys. Astron., 30, 1
Barnes D. J. et al., 2017b, MNRAS, 471, 1088
Beckwith S. V. W. et al., 2006, AJ, 132, 1729
Beers T. C., Flynn K., Gebhardt K., 1990, AJ, 100, 32
Bernardi M., Meert A., Sheth R. K., Vikram V., Huertas-Company M., Mei S., Shankar F., 2013, MNRAS, 436, 697
Bernardi M., Meert A., Vikram V., Huertas-Company M., Mei S., Shankar F., Sheth R. K., 2014, MNRAS, 443, 874
Bernardi M., Fischer J.-L., Sheth R. K., Meert A., Huertas-Company M., Shankar F., Vikram V., 2017, MNRAS, 468, 2569
Bertin E., 2009, Mem. Soc. Astron. Ital., 80, 422
Bertin E., 2013, PSFEx: Point Spread Function Extractor, Astrophysics Source Code Library, record ascl:1301.001
Bonafede A., Dolag K., Stasyszyn F., Murante G., Borgani S., 2011, MNRAS, 418, 2234
Borlaff A. et al., 2019, A&A, 621, A133
Bosch J. et al., 2018, PASJ, 70, S5
Brough S. et al., 2020, preprint (arXiv:2001.11067)
Bruzual G., Charlot S., 2003, MNRAS, 344, 1000
Burke C., Collins C. A., 2013, MNRAS, 434, 2856
Burke C., Collins C. A., Stott J. P., Hilton M., 2012, MNRAS, 425, 2058
Burke C., Hilton M., Collins C., 2015, MNRAS, 449, 2353
Chabrier G., 2003, PASP, 115, 763
Chambers K. C. et al., 2016, preprint (arXiv:1612.05560)
Ciotti L., 1991, A&A, 249, 99
Colless M. et al., 2001, MNRAS, 328, 1039
Collins C. A. et al., 2009, Nature, 458, 603
Contini E., De Lucia G., Villalobos Á., Borgani S., 2014, MNRAS, 437, 3787
Coupon J., Czakon N., Bosch J., Komiyama Y., Medezinski E., Miyazaki S., Oguri M., 2018, PASJ, 70, S7
Cui W. et al., 2014, MNRAS, 437, 816
Da Rocha C., Mendes de Oliveira C., 2005, MNRAS, 364, 1069
Da Rocha C., Ziegler B. L., Mendes de Oliveira C., 2008, MNRAS, 388, 1433
de Jong J. T. A., Verdoes Kleijn G. A., Kuijken K. H., Valentijn E. A., 2013, Exp. Astron., 35, 25
De Lucia G., Blaizot J., 2007, MNRAS, 375, 2
DeMaio T., Gonzalez A. H., Zabludoff A., Zaritsky D., Bradač M., 2015, MNRAS, 448, 1162
DeMaio T., Gonzalez A. H., Zabludoff A., Zaritsky D., Connor T., Donahue M., Mulchaey J. S., 2018, MNRAS, 474, 3009
Dolag K., Murante G., Borgani S., 2010, MNRAS, 405, 1544
Donzelli C. J., Muriel H., Madrid J. P., 2011, ApJS, 195, 15
Duc P.-A. et al., 2015, MNRAS, 446, 120
Ellien A., Durret F., Adami C., Martinet N., Lobo C., Jauzac M., 2019, A&A, 628, A34
Erfanianfar G. et al., 2019, A&A, 631, A175
Flaugher B., 2005, Int. J. Mod. Phys. A, 20, 3121
Furnell K. E. et al., 2018, MNRAS, 478, 4952
Gaia Collaboration, 2016, A&A, 595, A1
Gaia Collaboration, 2018, A&A, 616, A1
Giles P. A. et al., 2017, MNRAS, 465, 858
Gonzalez A. H., Zabludoff A. I., Zaritsky D., 2005, ApJ, 618, 195
Gonzalez A. H., Zaritsky D., Zabludoff A. I., 2007, ApJ, 666, 147
Gonzalez A. H., Sivanandam S., Zabludoff A. I., Zaritsky D., 2013, ApJ, 778, 14
Guglielmetti F., Fischer R., Dose V., 2009, MNRAS, 396, 165
Gunn J. E., Gott III J. R., 1972, ApJ, 176, 1
Guo Y. et al., 2009, MNRAS, 398, 1129
Guzzo L. et al., 2014, A&A, 566, A108
Harvey D., Courbin F., Kneib J. P., McCarthy I. G., 2017, MNRAS, 472, 1972
Hatch N. A. et al., 2011, MNRAS, 410, 1537
Henriques B. M. B., Thomas P. A., 2010, MNRAS, 403, 768
Hilton M. et al., 2018, ApJS, 235, 20
Hood R. J., Mann R. G., 2017, MNRAS, 469, 3851
Hu W., Kravtsov A. V., 2003, ApJ, 584, 702

Huang S. et al., 2018a, PASJ, 70, S6
Huang S., Leauthaud A., Greene J. E., Bundy K., Lin Y.-T., Tanaka M., Miyazaki S., Komiyama Y., 2018b, MNRAS, 475, 3348
Infante-Sainz R., Trujillo I., Román J., 2020, MNRAS, 491, 5317
Iodice E. et al., 2016, ApJ, 820, 42
Ivezic Z. et al., 2008, preprint (arXiv:0805.2366)
Jansen F. et al., 2001, A&A, 365, L1
Jedrzejewski R. I., 1987, MNRAS, 226, 747
Jiménez-Teja Y., Dupke R. A., 2015, Proc. 29th IAU General Assembly. Cambridge Univ. Press, Cambridge
Jiménez-Teja Y. et al., 2018, ApJ, 857, 79
Jiménez-Teja Y. et al., 2019, A&A, 622, A183
Jordi C. et al., 2010, A&A, 523, A48
Jurić M., Tyson T., 2012, Proc. IAU Vol. 10, Highlights H16: Highlights of Astronomy. p. 675
Kelvin L. S. et al., 2012, MNRAS, 421, 1007
Koposov S. E., Belokurov V., Torrealba G., 2017, MNRAS, 470, 2702
Krick J. E., Bernstein R. A., 2005, American Astronomical Society Meeting Abstracts, #177.14
Krick J. E., Bernstein R. A., 2007, AJ, 134, 466
Kron R. G., 1980, ApJS, 43, 305
Laporte C. F. P., White S. D. M., Naab T., Gao L., 2013, MNRAS, 435, 901
Lauer T. R. et al., 2007, ApJ, 664, 226
Lin Y.-T., Mohr J. J., 2004, ApJ, 617, 879
Lloyd-Davies E. J. et al., 2011, MNRAS, 418, 14
Lotz J. M. et al., 2017, ApJ, 837, 97
Lupton R., Gunn J. E., Ivezić Z., Knapp G. R., Kent S., 2001, in Harnden F. R., Jr, Primini F. A., Payne H. E., eds, ASP Conf. Ser. Vol. 238, Astronomical Data Analysis Software and Systems X. Astron. Soc. Pac., San Francisco, p. 269
McCarthy I. G., Bird S., Schaye J., Harnois-Deraps J., Font A. S., van Waerbeke L., 2018, MNRAS, 476, 2999
Mahdavi A., Hoekstra H., Babul A., Bildfell C., Jeltema T., Henry J. P., 2013, ApJ, 767, 116
Mancone C. L., Gonzalez A. H., 2012, PASP, 124, 606
Mehrtens N. et al., 2012, MNRAS, 423, 1024
Montes M., 2019, preprint (arXiv:1912.01616)
Montes M., Trujillo I., 2014, ApJ, 794, 137
Montes M., Trujillo I., 2018, MNRAS, 474, 917
Montes M., Trujillo I., 2019, MNRAS, 482, 2838
Morishita T., Abramson L. E., Treu T., Schmidt K. B., Vulcani B., Wang X., 2017, ApJ, 846, 139
Murante G., Giovalli M., Gerhard O., Arnaboldi M., Borgani S., Dolag K., 2007, MNRAS, 377, 2
Navarro J. F., Frenk C. S., White S. D. M., 1996, ApJ, 462, 563
Newman J. A. et al., 2013a, ApJS, 208, 5
Newman A. B., Treu T., Ellis R. S., Sand D. J., 2013b, ApJ, 765, 25
Peng C. Y., Ho L. C., Impey C. D., Rix H.-W., 2010, AJ, 139, 2097
Postman M. et al., 2012, ApJS, 199, 25
Presotto V. et al., 2014, A&A, 565, A126
Puchwein E., Springel V., Sijacki D., Dolag K., 2010, MNRAS, 406, 936
Ragone-Figueroa C., Granato G. L., Ferraro M. E., Murante G., Biffi V., Borgani S., Planelles S., Rasia E., 2018, MNRAS, 479, 1125
Román J., Trujillo I., Montes M., 2020, A&A, 644, A42
Romer A. K., Viana P. T. P., Liddle A. R., Mann R. G., 2001, ApJ, 547, 594
Rudick C. S., Mihos J. C., McBride C. K., 2011, ApJ, 732, 48
Scoville N. et al., 2007, ApJS, 172, 1
Seigar M. S., Graham A. W., Jerjen H., 2007, MNRAS, 378, 1575
Shan Y., McDonald M., Courteau S., 2015, ApJ, 800, 122
Slater C. T., Harding P., Mihos J. C., 2009, PASP, 121, 1267
Spavone M. et al., 2018, ApJ, 864, 149
Springel V. et al., 2005, Nature, 435, 629
Stott J. P. et al., 2010, ApJ, 718, 23
Tang L., Lin W., Cui W., Kang X., Wang Y., Contini E., Yu Y., 2018, ApJ, 859, 85
Toledo I., Melnick J., Selman F., Quintana H., Giraud E., Zelaya P., 2011, MNRAS, 414, 602
Trujillo I., Fliri J., 2016, ApJ, 823, 123
Uson J. M., Boughn S. P., Kuhn J. R., 1991, ApJ, 369, 46
Whiley I. M. et al., 2008, MNRAS, 387, 1253
Willman B., Governato F., Wadsley J., Quinn T., 2004, MNRAS, 355, 159
York D. G. et al., 2000, AJ, 120, 1579
Zacharias N., Monet D. G., Levine S. E., Urban S. E., Gaume R., Wycoff G. L., 2004, American Astronomical Society Meeting Abstracts, #48.15
Zhang Y. et al., 2019, ApJ, 874, 165
Zhao D., Aragón-Salamanca A., Conselice C. J., 2015a, MNRAS, 448, 2530
Zhao D., Aragón-Salamanca A., Conselice C. J., 2015b, MNRAS, 453, 4444
Zibetti S., White S. D. M., Schneider D. P., Brinkmann J., 2005, MNRAS, 358, 949
Zwicky F., 1937, ApJ, 86, 217
Zwicky F., 1952, PASP, 64, 242

APPENDIX A: ALTERNATIVE $k_{i,B}$-CORRECTION PARAMETERS

Table A1. The mean $k_{i,B}$-correction values for three formation redshifts z_f at three metallicity values (where $Z_\odot$ = solar) across all BC03 models for all sample clusters within $0 < z < 0.28$. The mean for the clusters used in this work is in the centre-left cell of this table.

	$Z = Z_\odot$	$Z = 0.4Z_\odot$	$Z = 2.5Z_\odot$
$z_f = 2$	−1.4409	−1.3203	−1.6470
$z_f = 3$	−1.4687	−1.3428	−1.6679
$z_f = 4$	−1.4811	−1.3531	−1.6822

Table A2. As in Table A1, but for clusters within $0.28 < z < 0.5$.

	$Z = Z_\odot$	$Z = 0.4Z_\odot$	$Z = 2.5Z_\odot$
$z_f = 2$	−1.2495	−1.1619	−1.4092
$z_f = 3$	−1.2735	−1.1755	−1.4127
$z_f = 4$	−1.2865	−1.1849	−1.4181

APPENDIX B: PARTIAL SPEARMAN ANALYSIS

Table B1. Partial Spearman analysis for the parameters discussed in Section 6, with $f_{\rm ICL}/f_{\rm tot}$ held constant.

	$f_{\rm ICL}/f_{\rm tot}$	$f_{\rm BCG}/f_{\rm tot}$	z	$\log_{10}M_{\rm X,500}$
$f_{\rm ICL}/f_{\rm tot}$	–	–	–	–
$f_{\rm BCG}/f_{\rm tot}$	–	–	−0.1448	−0.7493
z	–	−0.2467	–	0.3198
$\log_{10}M_{\rm X,500}$	–	−3.4625	−0.7082	–

Table B2. Partial Spearman analysis for the parameters discussed in Section 6, with $f_{\rm BCG}/f_{\rm tot}$ held constant.

	$f_{\rm ICL}/f_{\rm tot}$	$f_{\rm BCG}/f_{\rm tot}$	z	$\log_{10}M_{\rm X,500}$
$f_{\rm ICL}/f_{\rm tot}$	–	–	−0.7854	− 0.2215
$f_{\rm BCG}/f_{\rm tot}$	–	–	–	–
z	−3.9488	–	–	0.3687
$\log_{10}M_{\rm X,500}$	−0.4237	–	−0.8787	–

Table B3. Partial Spearman analysis for the parameters discussed in Section 6, with z held constant.

	$f_{\rm ICL}/f_{\rm tot}$	$f_{\rm BCG}/f_{\rm tot}$	z	$\log_{10}M_{\rm X,500}$
$f_{\rm ICL}/f_{\rm tot}$	–	−0.0642	–	0.1262
$f_{\rm BCG}/f_{\rm tot}$	−0.0969	–	–	− 0.7504
z	–	–	–	–
$\log_{10}M_{\rm X,500}$	−0.2091	−3.4767	–	–

Table B4. Partial Spearman analysis for the parameters discussed in Section 6, with $\log_{10}M_{\rm X,500}$ held constant.

	$f_{\rm ICL}/f_{\rm tot}$	$f_{\rm BCG}/f_{\rm tot}$	z	$\log_{10}M_{X,500}$
$f_{\rm ICL}/f_{\rm tot}$	–	−0.1139	−0.7791	–
$f_{\rm BCG}/f_{\rm tot}$	−0.1852	–	0.1829	–
z	−3.8577	−0.3301	–	–
$\log_{10}M_{X,500}$	–	–	–	–

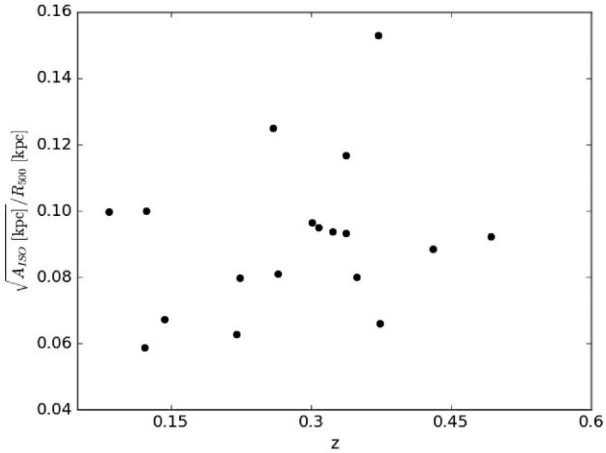

Figure C1. The square root of the isophotal area for each BCG against redshift, normalized by cluster radius. A Spearman rank reveals no strong correlation ($r_{\rm s} = 0.11$, $p = 0.66$).

APPENDIX C: TEST OF STELLAR POPULATION ON ICL-TO-BCG ASSIGNMENT DEPENDENCE

It was realized when carrying out the isophotal method of measuring ICL flux that choice of measurement band may potentially be a concern. Montes (2019) point out that measuring the ICL in bluer bands can lead to a stronger redshift trend than reality, due to the rapid fade of bluer stellar populations at high redshifts. Although we measure all clusters in the HSC *i* band, we *k*-correct to the *B* band, so performed a check on how this effect may influence our results via looking at the trend of the square root of the isophotal areas of the cluster BCGs (i.e. an approximation of the radius beyond which the ICL is considered for our clusters), normalized by the $R_{\rm X,500}$ value of each cluster (to account for cluster size) with redshift.

The result is shown in Fig. C1. There is a large amount of scatter, and the corresponding Spearman rank does not show evidence for a significant correlation here ($r_{\rm s} = 0.11$, $p = 0.66$). Studies with larger sample sizes may help clarify whether isophotal methods at different wavebands must consider this effect more carefully when interpreting their results.

This paper has been typeset from a TEX/LATEX file prepared by the author.